Dalton Transactions

ROYAL SOCIETY OF CHEMISTRY

PAPER

View Article Online
View Journal | View Issue

Check for updates

Cite this: *Dalton Trans.*, 2024, **53**, 2973

ATRP catalysts of tetradentate guanidine ligands – do guanidine donors induce a faster atom transfer?†‡

Konstantin W. Kröckert, Felix Garg, Joshua Heck, Michel V. Heinz, Justin Lange, Regina Schmidt, Alexander Hoffmann and Sonja Herres-Pawlis *

Tripodal tetradentate N donor ligands stabilise the most active ATRP catalyst systems. Here, we set out to synthesise the new guanidine ligand TMG-4NMe$_2$uns-penp, inspired by *p*-substituted tris(2-pyridylmethyl)amine (TPMA) ligands. The impact of changing pyridine against guanidine donors was examined through solid state and solution experiments and density functional theory (DFT) calculations. In the solid state, the molecular structures of copper complexes based on the ligands TMG-4NMe$_2$uns-penp, TMG-uns-penp and TMG$_3$tren were discussed concerning the influence of a NMe$_2$ substituent at the pyridines and the guanidine donors. In solution, the TMG-4NMe$_2$uns-penp system was investigated by several methods, including UV/Vis, EPR and NMR spectroscopy indicating similar properties to that of the highly active TPMA^{NMe2} system. The redox potentials were determined and related to the catalytic activity. Besides the expected trends between these and the ligand structures, there is evidence that guanidine donors in tripodal ligand systems lead to a better deactivation and possibly a faster exchange within the ATRP equilibrium than TPMA systems. Supported by DFT calculations, it derives from an easier cleavable Cu–Br bond of the copper(II) deactivator species. The high activity was stated by a controlled initiator for continuous activator regeneration (ICAR) ATRP of styrene.

Received 12th October 2023,
Accepted 3rd January 2024

DOI: 10.1039/d3dt03392a

rsc.li/dalton

Introduction

Since 1995,[1–4] atom transfer radical polymerisation (ATRP) has become a widespread method for controlled polymerisation owing to good tolerance to air using advanced ATRP techniques and the ability to synthesise polymers with a large variety of architectures.[5–7] In the ATRP mechanism exists a reversible equilibrium between the dormant and active radical species, which is usually mediated by a transition metal complex with a metal centre that is stable in at least two adjacent oxidation states. Many systems have been used, but copper complexes with multidentate N-donor ligands are the most successful and widely used ATRP catalysts.[8–12] The copper(I) activator complex ($Cu^{I}L_n$) reacts with the dormant radical chain or initiator (P–X) to yield the copper(II) deactivator complex (X–$Cu^{II}L_n$) and the active radical (P$^{\bullet}$) by homolytic cleavage of the C–X bond.[13] The radical can polymerise until the deactivator complex shifts the equilibrium back to the dormant side.[14] To suppress side reactions and maintain chain-end functionality, low radical concentrations and a reversible exchange of the equilibrium are necessary.[15,16] For standard ATRP, this can be achieved by the position of the equilibrium (K_{ATRP}) on the dormant side.[1,2] Contemporary ATRP variations such as mechanoATRP,[17,18] eATRP,[19,20] supplemental activators and reducing agents (SARA) ATRP,[21] photoATRP,[22–24] activators regenerated by electron transfer (ARGET) ATRP[25–27] and initiators for continuous activator

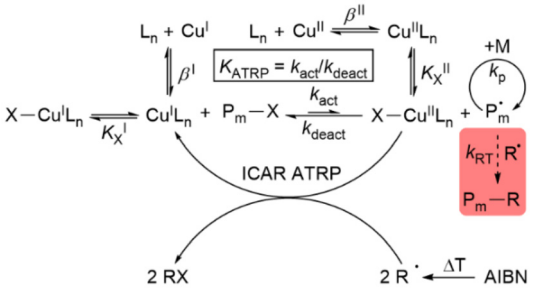

Scheme 1 Mechanism for ICAR ATRP with halidophilicity constants (K_X), stability constants (β) and unwanted radical side reactions (shaded red).[27]

Institute of Inorganic Chemistry, RWTH Aachen University, Landoltweg 1a, 52074 Aachen, Germany. E-mail: sonja.herres-pawlis@ac.rwth-aachen.de

†Electronic supplementary information (ESI) available. CCDC 2289693–2289698. For ESI and crystallographic data in CIF or other electronic format see DOI: https://doi.org/10.1039/d3dt03392a

‡Dedicated to Prof. Dr. Ulrich Simon on the occasion of his 60th birthday.

regeneration (ICAR) ATRP[27–30] (Scheme 1) allow good polymerisation control combined with a low catalyst loading. An increased ratio of the deactivator to activator complex is necessary to achieve this.[31,32] The reason for this is that a higher concentration of the deactivator complex improves the deactivation reaction, which has an effect on the dispersity.[31,32] Therefore, in contrast to standard ATRP, high K_{ATRP} values are essential for these methods. Because of this interrelation, K_{ATRP} is an expression for the catalyst activity.[33,34] Furthermore, the activator complex concentrations during the polymerisation should be low. This suppresses the formation of organometallic intermediates and the resulting radical termination (RT) reactions such as reductive radical terminations (RRT) and catalysed radical terminations (CRT), which increase the dispersity.[35,36]

Combining these properties with the listed activator regeneration techniques allows low amounts of catalysts down to parts per million levels and good control.[27,30] This simplifies purification steps and lowers costs. K_{ATRP}, the key value for catalyst activity, is correlated with the redox potential ($E_{1/2}$) for copper complexes with N donor ligands.[37,38] Low redox potentials lead to high K_{ATRP} values meaning a better stabilisation of the copper(II) complex. The activity can further be correlated with the stability constants β of the copper complexes. Here, it was found that K_{ATRP} values scale with the ratio of β^{II}/β^{I}. Large values for both constants are necessary, but β^{II} must be larger than β^{I} to induce a thermodynamic driving force for radical formation.[37,39,40] Additionally, the halidophilicity constant K_X^{II} is preferred to be large for efficient deactivation, and K_X^{I} should be low since $Cu^{I}L_n$ is required for activation.[41–44] Several studies highlighted trends of how the coordination sphere around the copper influences the catalyst activity.[45] The topology of the ligand, bridging units, denticity, the nature of the N donors, and here especially a high donor strength lead to an improvement.[38,46,47] These efforts have resulted in the most active ATRP systems to date, which are based on tetradentate NR_2 substituted tris(2-pyridylmethyl)amine (TPMA) ligands (an overview of the used abbreviations and the corresponding ligand structures can be found in ESI Fig. S18†).[27,30]

Guanidines exhibit excellent N donor properties and versatility.[48] Complexes with such ligands are not just suitable for ATRP[49–53] but also for ring-opening polymerisation,[53–55] oxygen activation,[56–58] model complexes for the entatic state of electron transfer proteins[59] and photochemistry.[60] Recently, we reported the most active ATRP catalyst based on a bidentate ligand, consisting of a NMe_2 substituted pyridine and a tetramethylguanidine (TMG) moiety (TMGm4NMe_2py).[61] It was found that structural features also caused by the guanidine function are the reason for the unexpected low redox potential and, therefore, high catalytic activity.

This study presents a novel guanidine ligand inspired by the most active tetradentate systems, but one pyridine donor is exchanged by one guanidine donor. Besides the aim to synthesise a highly active catalyst, we set out to investigate the influence of guanidine donors in tetradentate, tripodal ligands on the ATRP equilibrium.

Results and discussion

Ligand synthesis

Formal exchange of a pyridine unit of $TMPA^{NMe2}$ with the guanidine unit leads to the novel hybrid guanidine ligand TMG-4NMe_2uns-penp (**L1**). The synthesis is accomplished in three steps (Scheme 2). The literature-known compound 2-(1,3-dioxoisoindolin-2-yl)ethan-1-aminium 2,2,2-trifluoroacetate (**1**) was synthesised according to partly modified literature procedures from Franchini *et al.*,[62] Borovik *et al.*,[63] and Botta *et al.*[64] (Scheme S1†). By a reductive amination with the aldehyde (**2**) inspired by Britovsek *et al.*,[65] the new compound 2-(2-(bis((4-chloropyridin-2-yl)methyl)amino)ethyl)-isoindoline-1,3-dione (**3**) was received. In the next step, dimethylamine was inserted by nucleophilic aromatic substitution, and the phthalimide moiety was removed under basic conditions. The synthesis of amine **4** was inspired by a reaction of Matyjaszewski *et al.*[27] Finally, the guanidine ligand **L1** was obtained by a reaction of the amine precursor **4** with the Vilsmeier salt *N*,*N*,*N*′,*N*′-tetramethylchloroformamidinium chloride (TMG-VS).[66,67] The ligands TMG-uns-penp (**L2**, uns ≙ unsymmetric, penp ≙ pyridinyl-decorated ethylenediamine, uns-penp was originally reported by Mandel *et al.*[68]) and TMG_3tren (**L3**) were additionally selected for parts of this study to investigate the influence of electron density donating substituents and the number of guanidine donors on the catalyst structures and their redox potentials. These ligands were resynthesised according to the literature.[69,70]

Molecular structure in the solid state

The copper complexes [Cu(TMG-4NMe_2uns-penp)Br]Br (**C1**), [Cu(TMG-4NMe_2uns-penp)Cl]Cl (**C2**), [Cu(TMG-uns-penp)Br]Br·MeCN (**C3**), [Cu(TMG_3tren)Br]Br (**C4**) and [Cu(TMG_3tren)]Br·toluene (**C5**) were synthesised (Scheme 3) and their molecular structure in the solid state were examined *via* single crystal X-ray diffraction analysis. The molecular structures of the cation units in the solid state are presented in Fig. 1 and

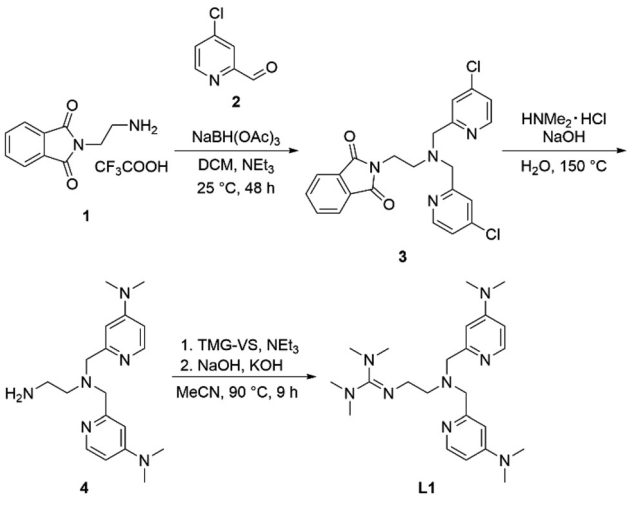

Scheme 2 Synthetic pathway for the ligand TMG-4NMe_2uns-penp (**L1**).

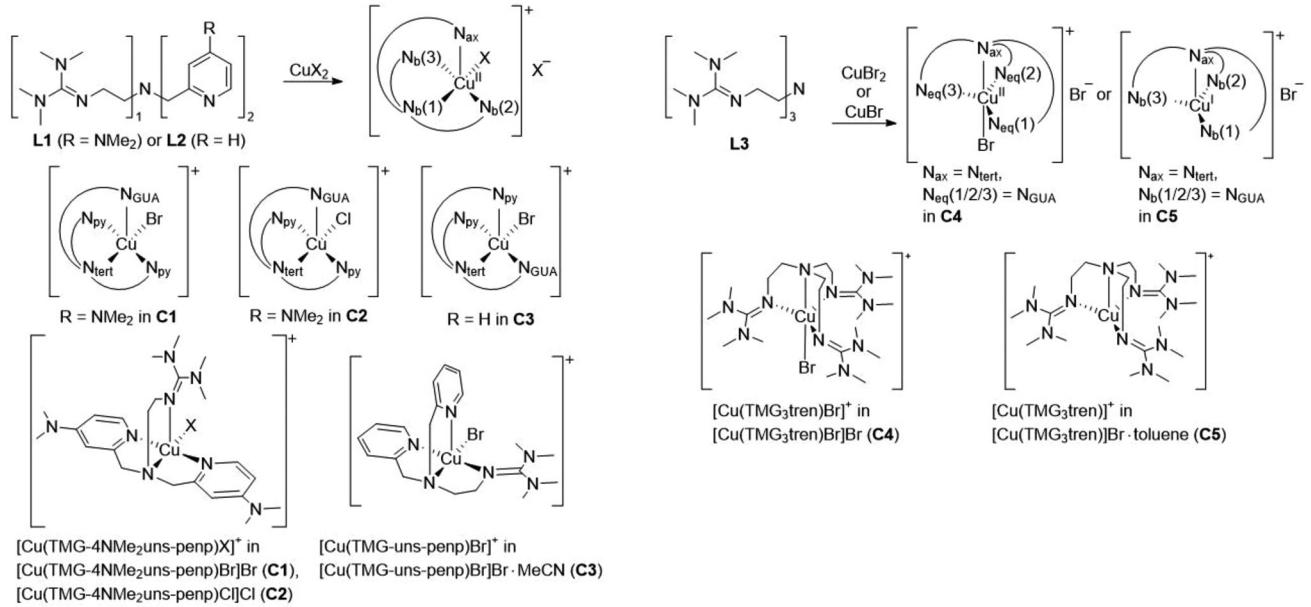

Scheme 3 Synthesis and schematic view of the molecular structure in the solid state of various copper complexes starting from the corresponding ligands **L1**, **L2** and **L3**. To clearly specify the N donors in axial, basal or equatorial position, the N donors were defined as follows: pyridine donor = N_{py}, TMG donor = N_{GUA}, tertiary N donor = N_{tert}.

selected bond lengths, angles, and geometrical factors are denoted in Table 1. Additional data can be found in the ESI (Fig. S1, S2 and Tables S1–S3†). The Cu(II) ions in the complex cations in **C1–C4** are fivefold coordinated by four N donor atoms and one halide atom, whereas the Cu(I) ion in the complex cation in **C5** is fourfold coordinated without a coordinating halide atom. The τ_5 value can be used to quantify the degree of distortion for fivefold coordinated systems and indicate ideal trigonal–bipyramidal coordination geometry for a value of 1 and an ideal square-pyramidal coordination geometry for a value of 0.[71] In the complex cations in **C1–C3**, the copper atoms are distorted square-pyramidal coordinated (τ_5 = 0.36–0.40) and the copper atom in the complex cation in **C4** is trigonal–bipyramidal coordinated (τ_5 = 1.01). The geometry of the fourfold coordinated copper atom can be described with the τ_4 value and the tetrahedral characteristic parameter (THC_{DA}).[72]

A τ_4 value of 1 indicates square-planar and a value of 0 indicates a tetrahedral coordination geometry. In contrast, the THC_{DA} value reaches 100 for tetrahedral structures and a value of 0 for trigonal-pyramidal structures. Therefore, the copper atom in the cationic complex unit in **C5** has a trigonal-pyramidal environment (τ_4 = 0.86, THC_{DA} = −16.2). The negative value can be explained with a smaller angle than 90° between the axial and basal donors.

In the complex cations in **C1** and **C2**, the NMe_2-substituted pyridine moieties, the tertiary amines, and the halides coordinate in the basal positions, and the guanidine is axially located. The Cu–N_b bond lengths to the same kind of donor in both complex cations in **C1** (N_b = N_{py} with 2.010(2) Å and 2.020 (2) Å and N_b = N_{tert} with 2.088(2) Å) and in **C2** (N_b = N_{py} with 2.009(2) Å and 1.999(2) Å and N_b = N_{tert} with 2.089(2) Å) are equal in the 3 σ confidence interval. The bond lengths to basal positions are shorter than the Cu–N_{ax} (N_{ax} = N_{GUA}) bond lengths equal in both complexes (in **C1**: 2.188(3) Å and in **C2**: 2.201(2) Å). The Cu–X bond length is larger for the bromide complex than for the chloride complex due to the larger ion

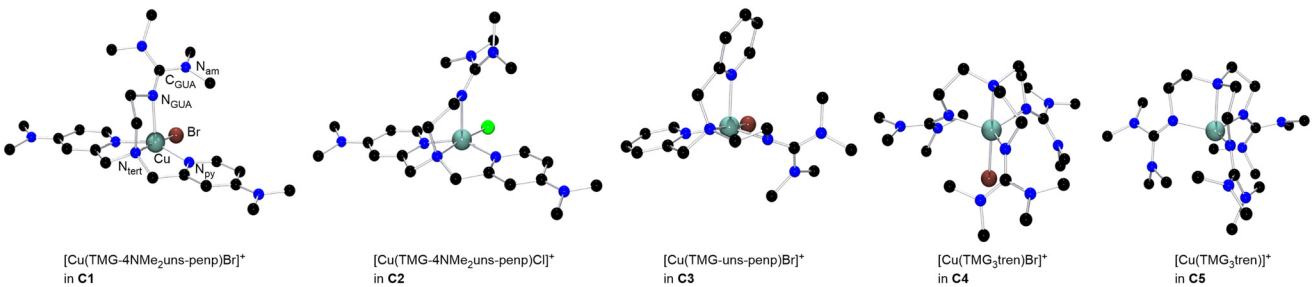

Fig. 1 Molecular structure of the cationic complex units in crystals of [Cu(TMG-4NMe$_2$uns-penp)Br]Br (**C1**), [Cu(TMG-4NMe$_2$uns-penp)Cl]Cl (**C2**), [Cu(TMG-uns-penp)Br]Br·MeCN (**C3**), [Cu(TMG$_3$tren)Br]Br (**C4**) and [Cu(TMG$_3$tren)]Br·toluene (**C5**) in the solid state. Key atoms are exemplarily marked in one complex and H atoms as well as non coordinating anions or solvent molecules are omitted for clarity.

Table 1 Key bond lengths, angles and geometrical factors of the complexes **C1**, **C2**, **C3**, **C4** and **C5**

Complex	**C1**	**C2**	**C3**	**C4** [a]	**C5**
Bond lengths [Å]					
Cu–N_{ax}	2.188(2); N_{ax} = N_{GUA}	2.201(2); N_{ax} = N_{GUA}	2.231(4); N_{ax} = N_{py}	2.112(3); N_{ax} = N_{tert}	2.200(2); N_{ax} = N_{tert}
Cu–$N_{b/eq}$ (1)	2.088(2); N_b = N_{tert}	2.089(2); N_b = N_{tert}	2.082(4); N_b = N_{tert}	2.061(3); N_{eq} = N_{GUA}	2.053(2); N_b = N_{GUA}
Cu–$N_{b/eq}$ (2)	2.010(2); N_b = N_{py}	2.009(2); N_b = N_{py}	1.970(4); N_b = N_{GUA}	2.065(3); N_{eq} = N_{GUA}	2.053(2); N_b = N_{GUA}
Cu–$N_{b/eq}$ (3)	2.020(2); N_b = N_{py}	1.999(2); N_b = N_{py}	2.031(4); N_b = N_{py}	2.138(3); N_{eq} = N_{GUA}	2.053(2); N_b = N_{GUA}
Cu–X	2.438(1); X = Br	2.282(1); X = Cl	2.394(1); X = Br	2.447(1); X = Br	—
C_{GUA}=N_{GUA}	1.308(4)	1.307(2)	1.328(5)	1.311 (av.)	1.305(2)
C_{GUA}–N_{am1}	1.367(4)	1.361(2)	1.339(6)	1.361 (av.)	1.380(2)
C_{GUA}–N_{am2}	1.366(4)	1.373(2)	1.360(5)	1.360 (av.)	1.374(2)
Bond angles [°]					
N_{ax}–Cu–X	101.9(1)	102.7(1)	99.4(1)	179.4(1)	—
$N_{b/eq}$ (1)–Cu–X	174.7(1)	174.5(1)	177.2(1)	98.8(1)	—
N_{ax}–Cu–$N_{b/eq}$ (1)	83.1(1)	82.7(1)	80.1(2)	81.8(2)	84.1(1)
N_{ax}–Cu–$N_{b/eq}$ (2)	107.7(1)	91.7(1)	95.6(2)	82.3(2)	84.1(1)
N_{ax}–Cu–$N_{b/eq}$ (3)	92.5(1)	108.0(1)	102.8(2)	81.8(2)	84.1(1)
$N_{b/eq}$ (1)–Cu–$N_{b/eq}$ (2)	82.2(1)	82.5(1)	84.0(2)	122.3(2)	119.0(1)
$N_{b/eq}$ (1)–Cu–$N_{b/eq}$ (3)	82.2(1)	82.0(1)	80.3(2)	113.1(2)	119.0(1)
$N_{b/eq}$ (2)–Cu–$N_{b/eq}$ (3)	152.6(1)	153.0(1)	153.3(2)	118.8(2)	119.0(1)
Geometrical factors					
τ_4 [b]/THC_{DA} [c]	—	—	—	—	0.86/−16.2
τ_5 [d]	0.37	0.36	0.40	1.01	—
ρ [e]	0.96	0.96	0.98	0.96	0.95

[a] Two crystallographic independent molecules are present in the asymmetric unit. Values for both are denoted in the ESI (Table S3†). [b] $\tau_4 = \frac{360° - (\alpha + \beta)}{141°}$. Ideal square-planar complexes generate a τ_4 value of 0 whereas ideal tetrahedral complexes generate a τ_4 value of 1.[72] [c] $THC_{DA} = \left(1 - \frac{\Sigma_n = 1 - 6|109.5° - \theta_n|}{90°}\right) \times 100$. The THC_{DA} value reaches 100 for ideal tetrahedral complexes and 0 for ideal trigonal–pyramidal complexes.[72] [d] $\tau_5 = \frac{(\alpha - \beta)}{60°}$. Ideal square-pyramidal complexes generate a τ_5 value of 0, whereas ideal trigonal–bipyramidal complexes generate a τ_5 value of 1.[71] [e] $\rho = \frac{2a}{(b + c)}$ with $a = d(C_{GUA}{=}N_{GUA})$ and b and $c = d(C_{GUA}{-}N_{am})$.[76]

radius. In the copper(II) bromide complex **C3** with the unsubstituted pyridine moieties, one of the pyridine donors is located in the axial position in contrast to **C1** where both pyridine donors coordinated in the basal position and the guanidine donor is located in the axial position. The other basal positions in **C3** are located with the other pyridine moiety, guanidine, bromide and the tertiary amine donor. All Cu–N bond lengths to basal located donors differ significantly due to the different donor characteristics but the Cu–N_{tert} bond lengths and the Cu–$N_{py,b}$ bond lengths are equal in **C1**–**C3**. The Cu–Br bond length in **C3** is shorter (Cu–Br = 2.394(1) Å) relative to the analogous bond lengths in **C1** (Cu–Br = 2.439(1) Å). The reason is the stronger electron density donating NMe_2 substituted pyridine unit that leads to a higher electron density at the copper centre (see DFT section).[73–75] Furthermore, the Cu–N_{ax} bond lengths for both substituted complexes are elongated compared to Cu–N_b bond lengths of the unsubstituted complex **C3**, indicating better coordination of the basal N donors. This is in accordance with a larger ρ value in **C3** (ρ = 0.98) than in **C1** (ρ = 0.96) due to the stronger coordination of the guanidine moiety. The ρ value reveals the delocalisation of the electrons within the guanidine function and is 1 for ideal delocalised systems.[76]

Compared to the complex cations in **C1**–**C3**, in the copper(II) bromide complex cation in **C4** the copper atom is trigonal–bipyramidal coordinated, despite the comparable ligand design. Two crystallographic independent molecules are present in the asymmetric unit (see Table S3†). Here the guanidine N donors coordinate in the equatorial positions (molecule 1: Cu–N_{eq} (1) = 2.061(3), Cu–N_{eq} (2) = 2.065(3), Cu–N_{eq} (3) = 2.138(3)); Molecule 2: Cu–N_{eq} (1) = 2.110(3), Cu–N_{eq} (2) = 2.100(3), Cu–N_{eq} (3) = 2.097(3) and the tertiary amine (molecule 1: Cu–N_{ax} = 2.112(3); molecule 2: Cu–N_{ax} = 2.113(3)) and the bromide (molecule 1: Cu–Br = 2.447(1); molecule 2: Cu–Br = 2.440(1)) are axially located. Three equal donors may be the reason for the change in the coordination geometry in the tripodal ligand structure, which was also observed in other copper complexes with three equal N donors.[77,78] The trigonal–bipyramidal structure with the tertiary amine and the bromide at the axial positions enables comparison to the structures of the copper(II) bromide complexes based on various TPMA ligands.[27,78,79] The average bond length to the equatorially located atoms is slightly increased for **C4** but more significant is the elongated bond length to the axially located atoms (Cu–Br = 2.447(1) Å, Cu–N_{tert} = 2.112(3) in **C4** *vs.* Cu–Br = 2.390(1) Å, Cu–N_{tert} = 2.047(3) in $TPMA^{NMe2}$ and Cu–

Br = 2.384(6) Å, Cu–N_{tert} = 2.040(3) in TPMA).[27,78,79] On the one hand, the longer Cu–Br bond length could indicate a lower halidophilicity of **C4** compared to the copper(II) TPMA systems, although it is required to form the deactivator complex in ATRP. On the other hand, a weaker and longer Cu–Br bond length could lead to an enhanced deactivation reaction. Furthermore, the only stable copper(I) bromide complex (**C5**) was received based on the ligand **L3**. The other systems tend to disproportionate and have a high sensitivity to air, similar to the highly active $TPMA^{NMe2}$-system.[27] The guanidine N donors in the Cu(I) complex **C5** coordinate in the basal positions (Cu–N_b (1) = 2.053(2), Cu–N_b (2) = 2.053(2), Cu–N_b (3) = 2.053(2)) and the bond lengths are shorter than of the axially located tertiary amine (Cu–N_{ax} = 2.200(2)). Analogous to previous studies for copper(I) complexes, the guanidine functions here are less delocalised (ρ = 0.95) compared to that in the copper(II) complexes.[49,80] The significant structural difference of the complex **C5** without a coordinating halide is notable to previously investigated ATRP systems based on the ligand TPMA where a halide is coordinating.[78] This can be interpreted as a better stabilisation of the required $Cu^{I}L_n$ activator species induced by the guanidine moieties.[42]

Structural studies in solution

In order to clarify the structure of the copper(I) and copper(II) complexes in solution, a titration experiment and UV/Vis, EPR, and variable temperature NMR spectroscopic experiments were exemplarily conducted based on ligand **L1**. Since the copper(I) bromide complex tends to disproportionate to elemental copper and the copper(II) complex, the titration experiment was only conducted for the copper(II) system. The intention is to show that in solution as well as in the solid-state the formation of a monochelate species is preferred. Copper(II) bromide was dissolved in MeCN, and aliquots of **L1** were added. Afterwards, the UV/Vis spectrum was obtained (Fig. S3†). The species formation was followed at 750 nm since the complex **C1** exhibits one maximum at this wavelength (Fig. 2). It increases linearly up to adding a half equivalent of **L1**, then decreases until one equivalent is reached. The course indicates that species distributions are present using insufficient amounts of ligand (less than 1 eq.). Presumably, there is the formation of a binuclear species with either two N donors of a ligand and two bromide ligands coordinating the copper or a species with two adjacent halogen-bridged copper centres. Nevertheless, a slight excess of ligand (more than 1 eq.) may ensure the presence of the monochelate complex. Thus, an equimolar amount or a slight excess of ligand is recommended for experiments with *in situ* formed complexes (Table 2).

UV/Vis spectra of the copper(II) bromide, chloride, and triflate complexes based on **L1** were recorded, and for all three complexes, two d–d transitions are obtained (Fig. 3). This is typical for copper(II) complexes coordinated by tetradentate ligand systems and has especially been observed for trigonal–bipyramidal copper(II) complexes. For these complexes, the transitions were related to the transitions $d_{x^2-y^2} \approx d_{xy} \rightarrow d_{z^2}$ and $d_{xz} \approx d_{yz} \rightarrow d_{z^2}$.[81,82] The transitions for **C1** are centred at 750 nm and 924 nm, for **C2** at 769 nm and 938 nm, and for [Cu(TMG-4NMe$_2$uns-penp)](OTf)$_2$ at 632 nm and 902 nm. There is a blue-shift depending on the anion for both transitions in the order OTf < Br < Cl. This is in accordance with the transitions of the published copper(II) bromide (776 nm and 1138 nm) and triflate (725 nm and 980 nm) complexes based on the ligand $TPMA^{NMe2}$.[27] The transitions presented here are blue-shifted; in particular, the first transition of the

Table 2 Extinction coefficients of selected copper(II) halide complexes in MeCN for their maxima between 500 and 1100 nm using the ratio CuX_2/L = 1/1

	λ_{max} [nm] (ε_{max} [L(mol cm)$^{-1}$])	
Complex	500–800 nm	800–1100 nm
[Cu(TMG-4NMe2uns-penp)Br]Br (**C1**)	750 (112)	942 (118)
[Cu(TMG-4NMe2uns-penp)Cl]Cl (**C2**)	757 (104)	945 (127)
[Cu(TMG-4NMe2uns-penp)](OTf)$_2$	632 (106)	911 (110)
[Cu($TPMA^{NMe2}$)Br]Br [27]	776 (n. d.)	1038 (n. d.)
[Cu($TPMA^{NMe2}$)](OTf)$_2$ [27]	725 (n. d.)	980 (n. d.)

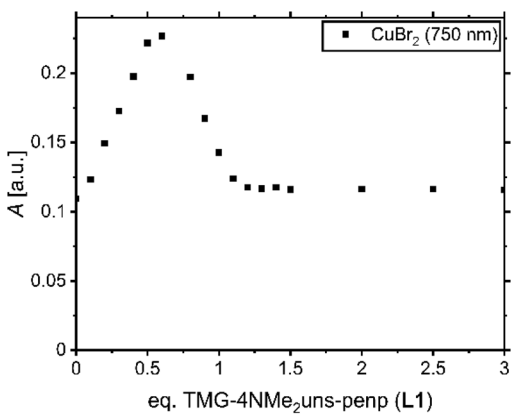

Fig. 2 UV/Vis spectroscopic titration of 5 mM $CuBr_2$ in MeCN with **L1**.

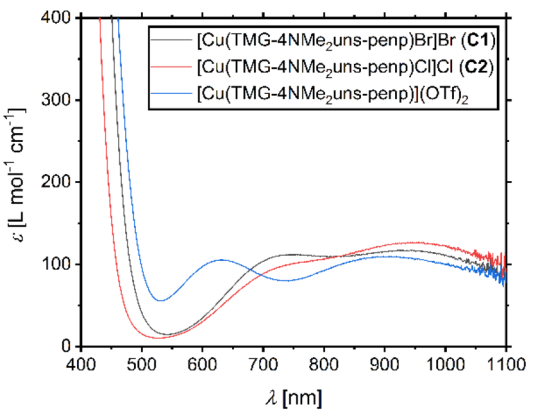

Fig. 3 UV/Vis spectra for 2.5 mM complex solutions in MeCN of [Cu(TMG-4NMe2uns-penp)Br]Br (**C1**), [Cu(TMG-4NMe2uns-penp)Cl]Cl (**C2**), and [Cu(TMG-4NMe2uns-penp)](OTf)$_2$.

triflate complex is very different. This indicates a significant influence of the guanidine moiety on the optical properties of these complexes and a larger gap in the orbital energy levels.

The complex **C1** was further exemplarily investigated by EPR spectroscopic measurements. In a DCM/toluene = 1/1 mixture, an axial spectrum was obtained (Fig. S5†). The EPR parameters could be simulated with the MATLAB tool EasySpin:[83] g_1 = 2.088, A_1 = 139 MHz, g_2 = 2.237, A_2 = 426 MHz, g_3 = 1.999 and A_3 = 193 MHz. The g and A parameters are similar to the analogue TPMA^{NMe2} complex in a DCM/toluene = 1/1 mixture: g_1 = 2.173, A_1 = 255.3 MHz, g_2 = 2.198, A_2 = 336.5 MHz, g_3 = 1.95 and A_3 = 260.1 MHz.[27] The slight differences could be explained by different structures analogous to the structures in the solid state. In MeCN it exhibits an isotropic spectrum (Fig. S4†) with a calculated cubic tensor of g_{iso} = 2.242. This is in an expected range compared to the tables of Peisach and Blumberg.[84] It is also similar to the measurement of the TPMA^{NMe2} based copper(II) bromide complex in MeCN with g_{iso} = 2.123.[27]

Furthermore, the properties of the catalyst system based on **L1** were characterised by variable temperature NMR spectroscopy. The intention is to show that this system undergoes fast ligand exchange in the presence of ligand excess relative to copper like other multidentate pyridine-based systems (Fig. 4 and Fig. S13†).[85] Analogous to the TPMA^{NMe2}-system, by using equimolar amounts of the ligand, the solution turned to a dark suspension due to a disproportionation reaction from [Cu(TMG-4NMe$_2$uns-penp)Br] to elemental copper, free ligand, and [Cu(TMG-4NMe$_2$uns-penp)Br]Br in acetone-d^6.[27] Acetone is a polar solvent that can interfere with the formation of the copper(II) deactivator complex and, thus, with the disproportionating properties of the copper(I) complex.[37] The reasons for this are its polarity and its weak coordination ability with copper(I). However, the main reason is the good stabilisation of the copper(II) centre by **L1**. Under ligand excess (**L1**/CuBr = 3/1), the disproportionation equilibrium is shifted to the copper(I) side. The previously paramagnetic dark suspension changed to a yellow diamagnetic solution, suitable for NMR spectroscopic investigations after a few minutes. At a temperature of 20 °C, the resonances are sharp and can be assigned in the aromatic region analogously to the resonances in the free ligand. The shifts vary slightly compared to the free ligand, but the coupling pattern of the protons is very similar. This indicates a fast exchange between the coordinated and the free ligand. By a decrease of temperature to −40 °C, the first broadening in the aromatic region was observed. This is reasoned by a slower rate of ligand exchange that continues to slow down at −80 °C. Here, the resonance of the proton c splits into separated resonance of free and coordinated ligand in an intensity ratio of 2/1. This behaviour is similar to that in previous investigated TPMA systems.[27,85]

Electrochemistry

The ATRP catalyst activity is described by the equilibrium constant which correlates to the redox potential for copper complexes with N donor ligands.[38] This allows the activity prediction of new catalyst systems solely on the basis of their redox potential.[27] Therefore, cyclic voltammetric measurements of the systems based on **L1–L3** were conducted (Fig. 5 and Fig. S6–S9†). The complexes were formed *in situ* dissolving equimolar amounts of ligand and copper(II) salt in acetonitrile at room temperature. The redox potential of the Fc/Fc$^+$ couple was subsequently measured and it served as an internal standard. Afterwards, the redox potentials of the systems were referred against saturated calomel electrode (SCE) for easier comparability with the literature.[86] The whole procedure was realised under a nitrogen atmosphere in a glovebox with degassed solvents to exclude oxygen, which is necessary due to

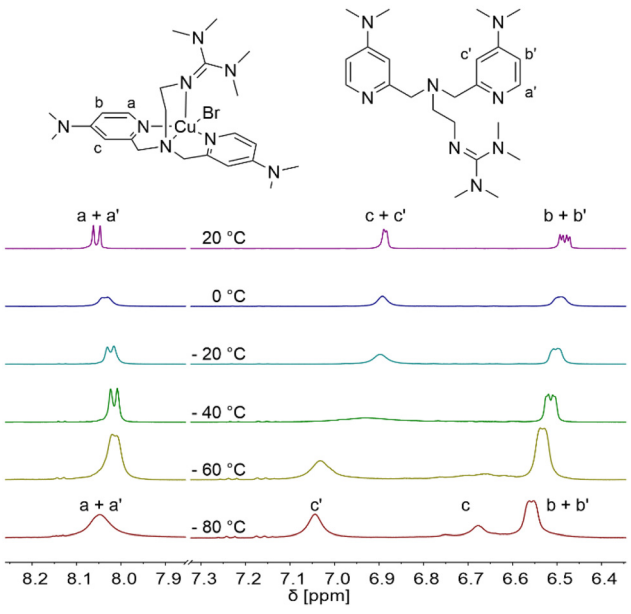

Fig. 4 Aromatic region of variable-temperature ^{1}H NMR spectra of the **L1**-based CuBr complex in d_6-acetone at a molar ratio of [CuBr] : [**L1**] = 1 : 3.

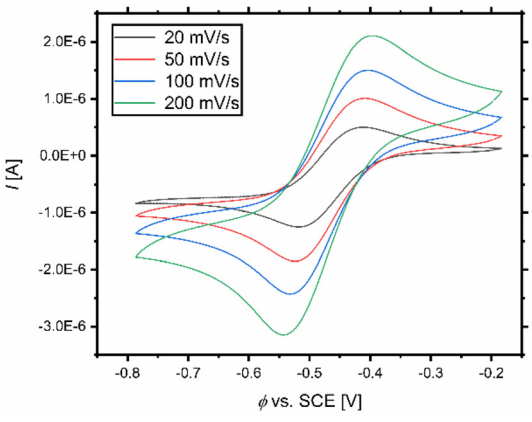

Fig. 5 Cyclic voltammograms with various scan rates of the Cu^{I}L/Cu^{II}L couple starting from a 1 mM [Cu(TMG-4NMe$_2$uns-penp)Br]Br complex solution in MeCN.

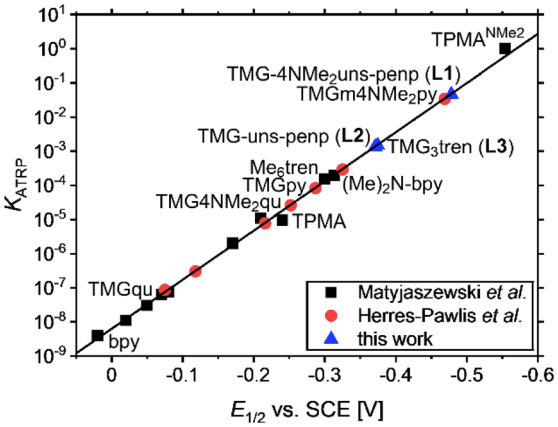

Fig. 6 Calculated K_{ATRP} values against measured $E_{1/2}$ values for various copper catalysts based on tetradentate guanidine ligands in the linear correlation of $E_{1/2}$ *vs.* log(K_{ATRP}).

the high air sensitivity of the catalyst systems. Scan rates of 200 mV s^{-1}, 100 mV s^{-1}, 50 mV s^{-1}, and 20 mV s^{-1} were used. The received values for $E_{1/2}$, the peak-to-peak separation (ΔE), and predicted K_{ATRP} values (predicted by using the correlation (Fig. 6))[38] are denoted in Table 3. The system based on **L1** and **L2** shows a reversible electron transfer (Tables S4–S7†). A quasi-reversible electron transfer for the systems based on **L3** explains the large values of ΔE (Table S8†).

It shows on the one side that these ligands can stabilise the electrochemically generated copper(I) complex, but on the other side that higher reorganisation energy for the systems based on **L1** and **L3** is required to change the geometry between the copper(II) and copper(I) complexes.[87] ΔE increases for ligands with dimethylaminepyridino (DMAP) units compared to pyridine units and for an increased number of TMG units.

It is consistent with the quasi-reversible nature of the electron transfer for the $TPMA^{NMe2}$ system[27] and a reversible electron transfer for the TPMA system.[38] For the system based on **L3**, a quasi-reversible redox wave with a peak-to-peak separation of ΔE = 440 mV was obtained.

A reason for the quasi-reversible behaviour in this magnitude could be the change in the coordination sphere by the redox process from the copper(I) complex without a coordinating halide to the copper(II) species with a coordinating halide like in the crystal structures. This change in the coordination geometry seems to be different relative to other comparable copper complexes with tripodal ligands like TPMA-based copper(I) complexes where a halide is coordinating.[78] To investigate the influence of the anion, measurements of the copper bromide, chloride, and triflate systems based on **L1** were conducted. The copper bromide system possesses a higher redox potential ($E_{1/2}$ = −0.478 V) relative to the appropriate copper chloride system ($E_{1/2}$ = −0.601 V) and a lower redox potential relative to the copper triflate system ($E_{1/2}$ = −0.373 V). This dependence on the halide is in accordance with the literature and indicates a higher redox potential by a larger Cu–X bond length.[49,88] The redox potential of the copper bromide system of **L1** ($E_{1/2}$ = −0.478 V) compared to that of **L2** ($E_{1/2}$ = −0.371 V) is lower due to the electron density donating dimethylamine moieties at the pyridines ($\Delta E_{1/2}$(**L1**/**L2**) = −0.107 V) leading to the most active ATRP catalyst based on a guanidine ligand (K_{ATRP} = 4.6 × 10^{-2}). The difference is smaller and in an expected range relative to the $TPMA^{NMe2}$ ($E_{1/2}$ = −0.554 V) and TPMA ($E_{1/2}$ = −0.240 V) systems since only two pyridines are substituted and not three ($\Delta E_{1/2}$($TPMA^{NMe2}$/TPMA) = −0.314 V). Notable is that the redox potential of the system based on **L2** is lower than that of the TPMA system indicating stronger electron density donating properties of the TMG unit relative to pyridine units. The influence of guanidine donors on activity is highly dependent on the ligand design, and the described increase in activities for the tetradentate pyridine ligands demonstrates the importance of studying these donors (Fig. 6). Advances in the ligand design lead to **L1**, which is the most reductive system based on guanidines to date. For the bromide system based on **L1**, the redox potential is higher and thus the activity is still lower relative to the system based on $TPMA^{NMe2}$ concerning larger K_{ATRP} values, but electrochemical differences influenced by the guanidine functions were found. The redox potential of the triflate system is lower ($E_{1/2}$ = −0.373 V with **L1** *vs.* $E_{1/2}$ = −0.302 V with $TPMA^{NMe2}$). The smaller difference in the redox potential of the bromide to the triflate system using the ligand **L1** compared to the $TPMA^{NMe2}$ ligand suggests less interference between halide and the copper centre induced by guanidine donors. A reason is a larger distance between the halide and the copper centre by the guanidine moiety. Lower redox potentials indicate a better copper(II) stabilisation and depend on the donating properties of the ligand.[27,89] In the triflate systems, the anion has less influence on the redox potential. Therefore, it reveals even more electron density donating properties of **L1** relative to the $TPMA^{NMe2}$ ligand and consequently stronger donating ability of TMG relative to DMAP moieties in these systems. The large peak-to-peak separation for the system based on **L3** can explain the similar $E_{1/2}$ values for the systems based on **L3** ($E_{1/2}$ = 0.375 V) and **L2** even though three donating TMG moieties are present in **L3**.

Using the redox potentials of the triflate system ($E_{1/2,LCu}$) based on **L1** and the previously determined standard redox potential of the solvated Cu^{I}/Cu^{II} couple in MeCN at T = 25 °C

Table 3 Redox potentials and derived K_{ATRP} values of various $Cu^{I}L/Cu^{II}L$ couples with L = **L1**–**L3**, $TPMA^{NMe2}$, and TPMA[27,38]

$Cu^{I}L/Cu^{II}L$, L=	X^-	$E_{1/2}$ *vs.* SCE [V]	ΔE [mV]	K_{ATRP}
TMG-4NMe$_2$uns-penp (**L1**)	Br^-	−0.478	99	4.6 × 10^{-2}
TMG-4NMe$_2$uns-penp (**L1**)	Cl^-	−0.601	79	—
TMG-4NMe$_2$uns-penp (**L1**)	OTf^-	−0.373	97	—
TMG-uns-penp (**L2**)	Br^-	−0.371	77	1.3 × 10^{-3}
TMG$_3$tren (**L3**)	Br^-	−0.375	440	1.5 × 10^{-3}
$TPMA^{NMe2}$ (ref. 27)	Br^-	−0.554	n. d.	≈1
$TPMA^{NMe2}$ (ref. 27)	OTf^-	−0.302	n. d.	—
TPMA (ref. 38)	Br^-	−0.240	70	9.6 × 10^{-6}

($E_{1/2,Cu}$ = 1.06°V *vs.* SCE), the β^{II}/β^{I} ratio can be calculated (eqn (1)).[27,42] The obtained value of $\beta^{II}/\beta^{I} = 1.7 \times 10^{24}$ is larger by one order of magnitude than of the TPMA^{NMe2}-system ($\beta^{II}/\beta^{I} = 1.1 \times 10^{23}$) revealing a huge driving force for copper(II) stabilisation and radical formation in ATRP. Furthermore, using the redox potential of the bromide system ($E_{1/2}$, LCuBr) the ratio of the apparent halidophilicity constants $K^{II}_{X,app}$, $K^{I}_{X,app}$ can be calculated (eqn (2)).

$$\ln\frac{\beta^{II}}{\beta^{I}} = \frac{F}{RT}(E_{1/2,Cu} - E_{1/2,LCu}) \quad (1)$$

$$\ln\frac{K^{II}_{X,app}}{K^{I}_{X,app}} = \frac{F}{RT}(E_{1/2,LCu} - E_{1/2,LCuBr}) \quad (2)$$

The received value of 60 is significantly lower than for the TPMA^{NMe2}-system (≈10^3). Since a good stabilisation of the activator complex by guanidine donors in tripodal and tetradentate ligands is proposed and the Cu–Br bond length is larger in the copper(II) complexes with guanidine moieties, this low value means a high stabilisation of the Cu^{II}L$_n$ species. Even though this is unwanted, it should lead to a large driving force for the activation reaction. Because the redox potential of the copper bromide system based on **L1** is higher relative to the TPMA^{NMe2} system and therefore K_{ATRP} is lower ($K_{ATRP} = 4.6 \times 10^{-2}$), concerning the relation $K_{ATRP} = k_{act}/k_{deact}$ the rate of deactivation must be even higher. Presumably well-stabilised species and the shifts of equilibria are highlighted in Scheme 4. Thus, there are indications that the guanidine moiety induces a faster exchange within the ATRP equilibrium. The reasons for this are better stabilisation of the copper(I) activator complex and improved deactivation by easier homolytic bond cleavage due to a larger Cu–Br bond length in the copper(II) deactivator complex.

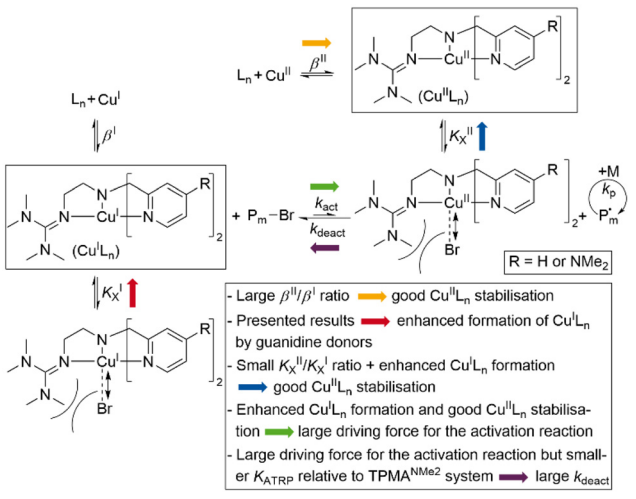

Scheme 4 Proposed impact of tetradentate guanidine ligands on ATRP equilibrium.

Density functional theory (DFT) calculations

DFT calculations were performed for the complex cations of **C1**, **C2**, **C3**, **C4**, **C5** and the related copper(II) bromide complexes based on the ligands TPMA and TPMA^{NMe2}. The functional TPSSh[90,91] and the basis set def2-TZVP[92–95] with a polarisable continuum model (PCM), as a solvent model for MeCN and empirical dispersion correction with the D3 version of Grimme's dispersion Becke–Johnson damping (GD3BJ) were used in accordance with previous studies (additional information is provided in the Experimental section).[96–98] Except for **C1**, the calculated complex structures by DFT are in agreement with the experimental ones (Fig. 7 and Tables S9–S12†). In **C1**, the N$_{tert}$–Cu–Br bond angle varies (174.7° *vs.* 163.8°), which explains the large difference in the τ_5 values (0.37 *vs.* 0.11). The calculated minimum of the calculation was thereby verified as described in the ESI† (DFT calculations of the complexes) and the slightly changed position of the bromide in the crystal structure was explained by packing effects.

In the following, the results for the copper(II) bromide complexes are discussed exclusively. The calculations reveal square-pyramidal structures for the complex cation in **C1** and **C3**, which correspond to the experimental structures. At this point, analogous to **C1**, the calculated minimum for **C3** was also verified as described in the ESI† in order to prove the exchange of the coordinating donors as a function of the dimethylamine substitution of the pyridine donors. Also corresponding to the experimental structures, trigonal–bipyramidal

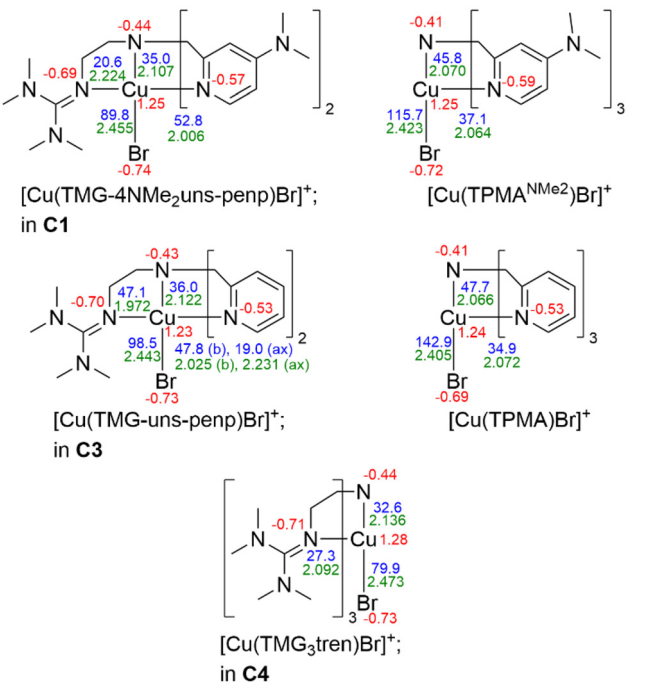

Fig. 7 Calculated NBO charges [e units] (red), charge-transfer energies E_{CT} [kcal mol^{-1}] (blue) and selected bond lengths [Å] (green) for selected Cu(II) deactivator complex cations (NBO7.0), TPSSh/def2-TZVP and PCM solvent model for MeCN and empirical dispersion correction with Becke–Johnson damping.

structures were obtained for the complex cation in **C4** and the copper(II) bromide complexes based on the ligands TPMA and $TPMA^{NMe2}$. For all structures, the trends between the calculated bond lengths are the same as for the experimentally determined structures and the root mean square deviation (RMSD) values are small.

The optimised structures were used for natural bond orbital (NBO) calculations to investigate the influence of the varied donors on the NBO charges of the copper, the donating N atoms, the coordinating bromide, and on the charge-transfer energies (E_{CT}). The NBO charge of the N donors decreases in the order: tertiary amine > pyridine > DMAP > guanidine, revealing the strongest basicity for the guanidine donor and the descending order of basicity within these systems.

In all complexes, E_{CT} are higher for DMAP *vs.* pyridine donors showing better donor properties of DMAP units due to electron density donating properties of the dimethylamine substituents. E_{CT} of the guanidine donors strongly depends on the complex geometry. As expected, E_{CT} of the axially located guanidine donor in the square-pyramidal complex cation in **C1** is lower than of the basally located guanidine in **C3**. Moreover, E_{CT} values of the equatorially located guanidine donors in the trigonal–bipyramidal complex cation in **C4** are lower than of those pyridine donors in the TPMA complexes, revealing weaker donation. The reason for this is the high steric demand of the bulky TMG moieties. The steric demand leads to interactions between the guanidines when three of these coordinate in the same plane, resulting in weaker donation despite their excellent donor properties.

It is proposed that a large Cu–Br bond length in the copper (II) deactivator complexes is easily cleavable homolytically, improving the deactivation reaction. In the calculated structures, the Cu–Br bond length for DMAP-containing complexes is elongated compared to the analogue pyridine complexes and even more by the number of guanidine donors, showing a dependence on the different donors as obtained in the crystal structures. Concerning E_{CT} of the bromide, there is a clear dependency on the N donors. E_{CT} of the bromide decreases by DMAP relative to unsubstituted pyridines, indicating that the Cu–Br bond gets weaker by stronger donating N donors.

This can be illustrated by the sum of the E_{CT} values of all coordinating N donors ($E_{CT,total}$). The value is higher for the copper(II) bromide $TPMA^{NMe2}$ complex ($E_{CT,total}$ = 156.9 kcal mol^{-1}) than for the comparable TPMA complex ($E_{CT,total}$ = 152.4 kcal mol^{-1}) and analogously when comparing the complexes in **C1** ($E_{CT,total}$ = 161.2 kcal mol^{-1}) and **C3** ($E_{CT,total}$ = 149.9 kcal mol^{-1}). The E_{CT} of the bromide also decreases by replacing a pyridine donor with a guanidine donor. In this case, the sum of the E_{CT} values of all coordinating N donors does not change significantly. Thus, certain electronic or steric properties of the guanidine must therefore be the reason that E_{CT} of the bromide decreases and consequently the bond is weakened. For the complex cation in **C4** with three guanidine donors, E_{CT} of the bromide is the lowest in the presented series. Since the interaction between the TMG units leads to a weaker donation of these and a lower sum of E_{CT} values of all coordinating N donors ($E_{CT,total}$ = 114.5 kcal mol^{-1}), the steric properties of the TMG moieties are mainly the reason for the low E_{CT} of the bromide in **C4**. However, there is evidence that the steric and the electronic properties of the guanidine donors are the reason for lower E_{CT} values of the bromide, and these correlate directly within these systems with the Cu–Br bond lengths. Therefore, the performed calculations show the bromide's weaker coordination in dependency of the N donors and emphasise the theory of a better cleavable Cu–Br bond by guanidine donors.

Polymerisation

The catalyst system based on **L1** contains a guanidine that leads to a weaker and elongated Cu–Br bond length in the deactivator complex and shows a very low redox potential with reversibility in the redox process comparable to that in the most active TPMA systems. Therefore, to assess the predicted high activity of this catalyst system the performance of standard ATRP and ICAR ATRP of styrene were tested. EBiB as initiator, AIBN as radical initiator and benzonitrile as solvent were used analogue to the conditions by previous studies.[49,52,61] The complexes were prepared *in situ* using copper(I) bromide and **L1** or copper(II) bromide and **L1** for

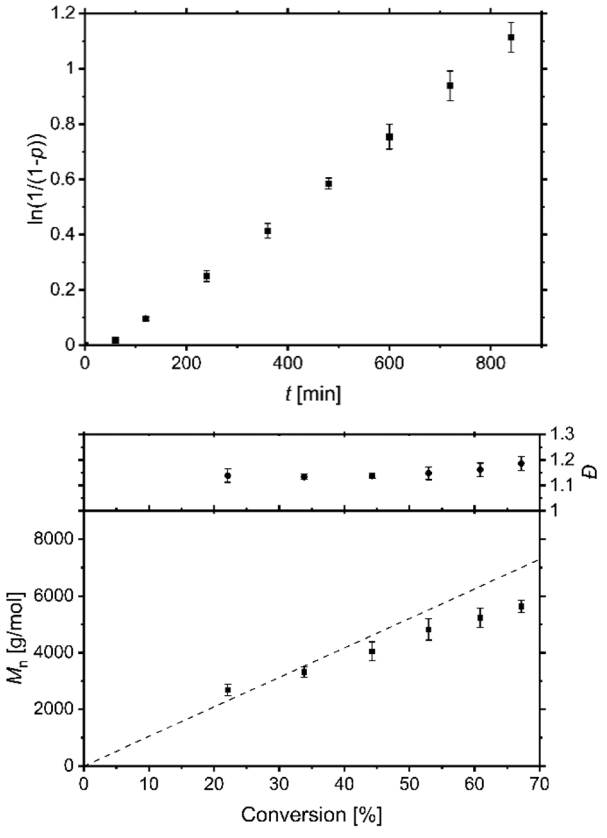

Fig. 8 Semilogarithmic plot of conversion *vs.* time (top) and plot of M_n/*Đ vs.* conversion (bottom) for ICAR ATRP of styrene with the $CuBr_2$/**L1** catalyst system. Conditions: Styrene//EBiB/Cat./AIBN = 100/1/0.1/1.5 in benzonitrile at 60 °C.

Table 4 Conversions, molar masses and dispersity for ICAR ATRP of styrene in benzonitrile with EBiB as initiator and AIBN as reducing agent using the $CuBr_2$/**L1**, $CuBr_2$/**L3** and $CuBr_2$/TPMA catalyst systems with a ratio of styrene/EBiB/Cat./AIBN = 100/1/0.5/1.5 at 60 °C

	TMG-4NMe$_2$uns-penp (**L1**)				TMG$_3$tren (**L3**)				TPMA			
t [h]	p [%]	M_n [g mol^{-1}]	$M_{n,th}$ [g mol^{-1}]	$Đ$	p [%]	M_n [g mol^{-1}]	$M_{n,th}$ [g mol^{-1}]	$Đ$	p [%]	M_n [g mol^{-1}]	$M_{n,th}$ [g mol^{-1}]	$Đ$
1	2	n. d.	200	n. d.	1	n. d.	100	n. d.	0	n. d.	0	n. d.
2	9	n. d.	900	n. d.	8	n. d.	800	n. d.	1	n. d.	100	n. d.
4	22	2700	2300	1.14	23	1700	2400	1.19	16	n. d.	1700	n. d.
6	34	3300	3500	1.13	35	2400	3700	1.17	29	1700	3000	1.10
8	44	4100	4600	1.14	46	2800	4800	1.18	40	2500	4200	1.09
10	53	4800	5500	1.15	55	3800	5700	1.13	50	3000	5200	1.09
12	61	5200	6400	1.16	62	3700	6500	1.18	57	3200	5900	1.12
14	67	5600	7000	1.19	67	4000	7000	1.19	63	3600	6600	1.12

standard ATRP or ICAR ATRP experiments, respectively. The performance of standard ATRP with a ratio of M/I/Cat. = 100/1/1 was tested but indicates an uncontrolled behaviour (Fig. S15†). A reason is the low redox potential resulting in a high amount of copper(II) species and free radicals. That causes more radical terminations, a change of radical concentration, and a polymerisation not following pseudo-first-order kinetics. In contrast, using a ratio of M/I/Cat./AIBN = 100/1/0.1/1.5 at 60 °C, a linear increase of the semilogarithmic plot of conversion *vs.* time was observed (Fig. 8) indicating a successful ICAR ATRP. To quantify the results, polymerisations were also carried out under analogous conditions, but with the ligands **L3** and TPMA (Fig. S16 and S17†). The rate constants k_{obs} depend on the AIBN concentration and the rate of decomposition.[10,32,99] The values (**L1**: $k_{obs} = 1.4 \times 10^{-3} \pm 1.6 \times 10^{-5}$ s^{-1}; **L3**: $k_{obs} = 1.5 \times 10^{-3} \pm 1.2 \times 10^{-5}$ s^{-1}; **TPMA**: $k_{obs} = 1.4 \times 10^{-3} \pm 2.3 \times 10^{-5}$ s^{-1}) are very similar to previous results from us using comparable conditions ($k_{obs} = 1.3 \times 10^{-3} \pm 2.2 \times 10^{-5}$ s^{-1}).[52,61] The short induction period at the beginning may be explained by radical consumption of the deactivator complex until a specific ratio of activator to deactivator is reached.

The controlled behaviour of the polymerisations were confirmed by the constant growth of the molar masses that fit to the expected ones and low dispersities by increased conversions up to 67% after 14 h for the system based on **L1** (Table 4). This practical example underlines the excellent mediator properties of the catalyst system based on **L1**, even if the comparative experiments with **L3** and TPMA show that under these conditions there is barely any difference in polymerisation behaviour with regard to dispersity. However, the conversion increases faster for **L1** and **L3** in these ICAR ATRP experiments compared to TPMA. The main reason for this is the low redox potential and a high value for K_{ATRP}, which promote activation, but due to successful deactivation and a high amount of copper(II) deactivator species, the dispersities are still low.[31,32] A high value for the equilibrium constant can also be a reason for low dispersity due to the decrease of unwanted side reactions such as CRT and RRT.[35,36] The elongation of the Cu–Br bond length in the deactivator complex and the resulting presumed faster exchange within the equilibrium by guanidine donors may also have an influence.

Conclusions

The synthetic pathway for the novel ligand TMG-4NMe$_2$uns-penp (**L1**) is presented. Besides **L1**, the tripodal and tetradentate ligands TMG-uns-penp (**L2**) and TMG$_3$tren (**L3**) were used to investigate the influence of guanidine moieties on the ATRP catalyst properties. With these ligands, copper complexes were synthesised and crystallised for structure analysis in the solid state. Based on **L1** and **L2**, distorted square-pyramidal complexes were obtained, and it was found that the position of the guanidine N donor changes by NMe_2 substitution at the pyridines. Based on **L3**, a trigonal–bipyramidal structure that can be related to the TPMA systems was received. Guanidine donors increased the bond lengths between the copper centre and the bromide ligand. This is underlined by the trigonal–pyramidal copper(I) complex based on **L3** without a coordinating halide which is different in the copper(I) halide complexes based on the TPMA ligand where the halide coordinates. Additionally, this system does not disproportionate despite the strong donating guanidine donors. Thus, the stabilisation of the activator complex by the guanidine moieties in tripodal ligands seems to be higher.

The catalyst activities for the systems based on **L1–L3** were predicted by measurements of the redox potentials and using the strong correlation with K_{ATRP}. As expected, dimethylamine substituents at the pyridines lead to a lower redox potential, making the system based on **L1** the most active ATRP catalyst based on a guanidine ligand ($E_{1/2} = -0.478$ V *vs.* SCE, $K_{ATRP} = 4.6 \times 10^{-2}$). Moreover, based on the measured redox potentials, an overall faster exchange within the ATRP equilibrium was derived, which could be important for future polymerisations in terms of low dispersity.[100] The reasons proposed are the preferential presence of the activator complex and a weaker Cu–Br bond in the deactivator complex that could improve the deactivation reaction. An elongated Cu–Br bond length and its weakening by guanidine units are supported by DFT calculations. A successful ICAR ATRP of styrene indicated high

activity and good reversibility within the ATRP equilibrium. Controlled conditions with low dispersities and molar masses that fit to the expected ones were obtained. This shows the large potential of guanidine copper systems in ATRP and opens up new avenues in ligand design for CRP methods.

Experimental part

General information

The synthesis of the ligands and complexes was conducted under inert conditions under a nitrogen atmosphere (99.999% purity) using the Schlenk technique or a glovebox. Purified and degassed solvents were used and were purified according to the literature.[101] The chemicals for the synthesis of the ligands and complexes were all purchased from ABCR, Acros Organics, Alfa Aesar, Grüssing, Fluka Analytical, Fisher-Scientific, Sigma-Aldrich or TCI and were used as received without further purification. The compounds 2-(1,3-dioxoisoindolin-2-yl)ethan-1-aminium 2,2,2-trifluoroacetate (**1**) and 4-chloropicolinaldehyde (**2**) were resynthesised by modifying the literature procedures, which is described in the ESI.†[64,102] The Vilsmeier salt *N*,*N*,*N*′,*N*′-tetramethylchloroformamidinium chloride (TMG-VS), copper(I) bromide, **L2** and **L3** were synthesized as described in the literature.[67,69,70,103]

Ligand synthesis

2-(2-(Bis((4-chloropyridin-2-yl)methyl)amino)ethyl)isoindoline-1,3-dione (3).[65]

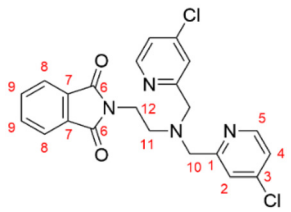

2-(1,3-Dioxoisoindolin-2-yl)ethan-1-aminium 2,2,2-trifluoroacetate (10.0 g, 32.9 mmol, 1 eq.), triethyl amine (3.33 g, 32.9 mmol, 1 eq.) and 4-chloropicolinaldehyde (9.31 g, 65.8 mmol, 2 eq.) were dissolved in DCM (200 mL) and stirred for 1 h. To this solution sodium tri(acetoxy)borohydride (20.9 g, 98.7 mmol, 3 eq.) and DCM (100 mL) were added and the suspension was stirred for 18 h. After that, the mixture was quenched with saturated sodium hydrogen carbonate solution, the organic layer was separated, and the aqueous phase was extracted with DCM (2 × 150 mL). The combined organic layers were dried over $MgSO_4$ and the solvent was removed under reduced pressure. For purification, the product was diluted in DCM (10 mL) and slowly added to *n*-hexane (300 mL). The precipitate was filtered and residual solvent removed under reduced pressure (yield = 98%, 14.2 g, 32.2 mmol). **^{1}H NMR** (400 MHz, $CDCl_3$): δ = 8.32 (d, $^3J_{HH}$ = 5.4 Hz, 2H, CH, 5), 7.83 (m, 2H, CH, 8), 7.73 (m, 2H, CH, 9), 7.31 (d, $^4J_{HH}$ = 2.0 Hz, 2H, CH, 2), 7.08 (dd, $^3J_{HH}$ = 5.4, $^4J_{HH}$ = 2.0 Hz, 2H, CH, 4), 3.85 (m, 6H, CH_2, 10 + 11), 2.89 (t, $^3J_{HH}$ = 5.9 Hz, 2H, CH_2, 12) ppm. **^{13}C NMR** (101 MHz, $CDCl_3$): δ = 168.4 (C_q, 7), 161.0 (C_q, 1), 149.9 (CH, 5), 144.7 (C_q, 3), 134.1 (CH, 9), 132.2 (C_q, 6), 123.5 (CH, 8), 123.4 (CH, 2), 122.6 (CH, 4), 59.8 (CH_2, 10), 51.9 (CH_2, 12), 35.9 (CH_2, 11) ppm. **IR** (Diamond-ATR, neat) $\tilde{\nu}_{max}$: 3025 (vw), 2946 (vw), 2855 (vw), 1765 (m), 1706 (vs), 1679 (w), 1575 (m), 1555 (m), 1468 (w), 1454 (w), 1426 (m), 1393 (s), 1366 (m), 1352 (m), 1323 (m), 1280 (w), 1250 (vw), 1215 (w), 1186 (m), 1172 (w), 1133 (w), 1108 (m), 1087 (m), 1036 (w), 1019 (w), 981 (w), 970 (m), 955 (w), 940 (m), 895 (w), 875 (w), 862 (w), 825 (m), 802 (w), 739 (m), 720 (vs), 703 (s), 670 (m), 606 (w), 573 (w), 544 (w), 530 (m), 494 (w), 457 (m), 428 (s), 406 (w), 369 (w), 354 (s), 331 (m) cm^{-1}. **HRMS** (ESI^+, MeOH) *m*/*z*: isotopic distribution calcd for $C_{22}H_{19}N_4Cl_2O_2$ $[M + H]^+$: 441.0886 (100) $[C_{22}H_{19}{}^{35}Cl_2N_4O_2]^+$, 442.0915 (26) $[C_{21}{}^{13}CH_{19}{}^{35}Cl_2N_4O_2]^+$, 443.0864 (68) $[C_{22}H_{19}{}^{35}Cl^{37}ClN_4O_2]^+$, 444.0890 (17) $[C_{21}{}^{13}CH_{19}{}^{35}Cl^{37}ClN_4O_2]^+$, 445.0839 (13) $[C_{22}H_{19}{}^{37}Cl_2N_4O_2]^+$, 446.0862 (3) $[C_{21}{}^{13}CH_{19}{}^{37}Cl_2N_4O_2]^+$; found: 441.0887 (100), 442.0920 (26), 443.0857 (68), 444.0887 (16), 445.0825 (11), 446.0855 (3).

Additional information on the synthesis of the target compound and original analysis data files are available *via* Chemotion Repository: **https://dx.doi.org/10.14272/reaction/SAFUHFF-UHFFFADPSC-MBUHWDDXOF-UHFFFADPSC-NUHFF-NUHFF-NUHFF-ZZZ**.

***N*^{1},*N*^{1}-Bis((4-(dimethylamino)pyridin-2-yl)methyl)ethane-1,2-diamine (4).[27]**

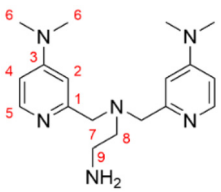

2-(2-(Bis((4-chloropyridin-2-yl)methyl)amino)ethyl)isoindoline-1,3-dione (6.88 g, 15.9 mmol, 1 eq.) and dimethylamine hydrochloride (16.0 g, 196 mmol, 12.3 eq.) were added to a 100 mL pressure flask. Water (50 mL) was added and then NaOH (7.82 g, 196 mmol, 12.3 eq.) was added and the flask was quickly closed. The mixture was stirred at 150 °C overnight. The cooled flask was opened and the mixture was diluted with 1 M NaOH (200 mL) and was stirred for 2 h. The solution was extracted with MeCN (3 × 150 mL), the combined organic layers were dried over Na_2SO_4, filtered and the solvent evaporated under reduced pressure. The product was used for following synthesis without further purification. (Yield = 67%, 3.50 g, 10.7 mmol). **^{1}H NMR** (400 MHz, $CDCl_3$): δ = 8.09 (d, $^3J_{HH}$ = 5.9 Hz, 2H, CH, 5), 6.73 (d, $^4J_{HH}$ = 2.4 Hz, 2H, CH, 2), 6.31 (dd, $^3J_{HH}$ = 5.9 Hz, $^4J_{HH}$ = 2.4 Hz, 2H, CH, 4), 3.69 (s, 4H, CH_2, 7), 2.93 (s, 12H, CH_3, 6), 2.74 (t, J = 5.8 Hz, 2H, CH_2, 9), 2.63 (t, J = 5.8 Hz, 2H, CH_2, 8), 2.44 (br. s, 2H, NH_2) ppm. **^{13}C NMR** (101 MHz, $CDCl_3$): δ = 159.7 (C_q, 1), 154.9 (C_q, 3), 149.1 (CH, 5), 105.5 (CH, 2), 105.2 (CH, 4), 61.2 (CH_2, 7), 57.6 (CH_2, 8), 39.8 (CH_2, 9), 39.1 (CH_3, 6) ppm. **IR** (Diamond-ATR, neat) $\tilde{\nu}_{max}$: 3353 (vw, ν(N–H)), 2896 (w), 2819 (w), 1596 (vs), 1540 (m), 1507 (m), 1449 (m), 1433 (m), 1373 (m), 1310 (w), 1269 (w),

1220 (m), 1163 (w), 1130 (w), 1110 (w), 1068 (w), 1003 (m), 984 (m), 968 (m), 881 (w), 841 (w), 806 (m), 766 (w), 740 (w), 599 (vw), 482 (vw), 441 (vw), 318 (vw) cm^{-1}. **HRMS** (ESI^+, MeOH) *m*/*z*: isotopic distribution calcd for $C_{18}H_{29}N_6$ $[M + H]^+$: 329.2453 (100) $[C_{18}H_{29}N_6]^+$, 330.2483 (22) $[C_{17}{}^{13}CH_{29}N_6]^+$, 331.2508 (2) $[C_{16}{}^{13}C_2H_{29}N_6]^+$; found: 329.2449 (100), 330.2481 (21), 331.2514 (2).

Additional information on the synthesis of the target compound and original analysis data files are available *via* Chemotion Repository: **https://dx.doi.org/10.14272/reaction/SA-FUHFF-UHFFFADPSC-WNSOFCUINP-UHFFFADPSC-NUHFF-NUHFF-NUHFF-ZZZ**.

2-(2-(Bis((4-(dimethylamino)pyridin-2-yl)methyl)amino) ethyl)-1,1,3,3-tetramethylguanidine (TMG-4NMe$_2$uns-penp, L1) [synthesised analogously to the standard guanidine synthesis protocol].[66,67]

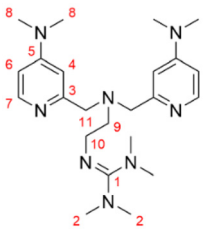

N^1,N^1-Bis((4-(dimethylamino)pyridin-2-yl)methyl)ethane-1,2-diamine (6.00 g, 18.3 mmol, 1 eq.) and triethylamine (2.22 g, 21.9 mmol, 1.2 eq.) were dissolved in acetonitrile (130 mL) and the TMG-VS (3.75 g, 21.9 mmol, 1.2 eq.) in acetonitrile (30 mL) was slowly added at room temperature to the reaction mixture. After refluxing for 3 h, the mixture was cooled to room temperature. An aqueous solution of sodium hydroxide (0.88 g, 21.9 mmol, 1.2 eq.) was added and triethylamine as well as the solvents were removed under reduced pressure. A 50% solution of potassium hydroxide in water (50 mL) was added and the product was extracted with acetonitrile (3 × 150 mL). The combined organic layers were dried over Na_2SO_4. Activated charcoal was added and after filtration over Celite®, the solvent was removed under reduced pressure and the raw product was obtained (97%, 7.64 g, 17.9 mmol). For purification, toluene was added to the raw product and refluxed under stirring for 10 min. The hot toluene phase was decanted and the solvent was removed under reduced pressure. To the light brown oil, *n*-heptane was added and refluxed for 10 min. The hot *n*-heptane phase was decanted and the product crystallised overnight. The bright yellow crystals were dispersed, filtered and dried under reduced pressure (24%, 1.86 g, 4.36 mmol). **^{1}H NMR** (400 MHz, $CDCl_3$): δ = 8.08 (d, $^3J_{HH}$ = 5.9 Hz, 2H, CH, 7), 6.86 (d, $^4J_{HH}$ = 2.7 Hz, 2H, CH, 4), 6.30 (dd, $^3J_{HH}$ = 5.9 Hz, $^4J_{HH}$ = 2.7 Hz, 2H, CH, 6), 3.76 (s, 4H, CH_2, 11), 3.37–3.24 (m, 2H, CH_2, 10), 2.93 (s, 12H, CH_3, 8), 2.81–2.73 (m, 2H, CH_2, 9), 2.65 (s, 6H, CH_3, 2), 2.59 (s, 6H, CH_3, 2) ppm **^{13}C NMR** (101 MHz, $CDCl_3$): δ = 160.5 (C_{GUA}, 1), 160.5 (C_q, 3), 155.0 (C_q, 5), 149.1 (CH, 7), 105.2 (CH, 4), 105.1 (CH, 6), 61.3 (CH_2 11), 57.4 (CH_2, 9), 47.6 (CH_2, 10), 39.7 (CH_3, 2), 39.1 (CH_3, 8), 39.0 (CH_3, 2) ppm. **IR** (Diamond-ATR, neat) $\tilde{\nu}_{max}$: 2929 (w, $\nu(CH_{aliph.})$), 2888 (w, $\nu(CH_{aliph.})$), 2812 (w), 1613 (s), 1597 (vs, ν(C=N)), 1541 (m), 1504 (m), 1444 (m), 1428 (m), 1413 (w), 1362 (s), 1313 (w), 1288 (w), 1267 (w), 1235 (m), 1219 (m), 1162 (w), 1128 (m), 1107 (w), 1081 (w), 1069 (w), 1010 (m), 952 (w), 920 (w), 894 (w), 878 (w), 850 (m), 823 (w), 807 (s), 739 (w), 662 (vw), 638 (vw), 593 (w), 578 (w), 537 (vw), 481 (w), 452 (w), 394 (w) cm^{-1}. **HRMS** (ESI^+, MeOH) *m*/*z*: isotopic distribution calcd for $C_{23}H_{39}N_8$ $[M + H]^+$: 427.3299 (100) $[C_{23}H_{39}N_8]^+$, 428.3327 (28) $[C_{22}{}^{13}CH_{39}N_8]^+$, 429.3350 (4) $[C_{22}{}^{13}C_2H_{39}N_8]^+$; found: 427.3302 (100), 428.3322 (50), 429.3350 (6).

Additional information on the synthesis of the target compound and original analysis data files are available *via* Chemotion Repository: **https://dx.doi.org/10.14272/reaction/SA-FUHFF-UHFFFADPSC-QPLGYGHVGP-UHFFFADPSC-NUHFF-NUHFF-NUHFF-ZZZ**.

Complex synthesis

[Cu(TMG-4NMe$_2$uns-penp)Br]Br (C1). TMG-4NMe$_2$uns-penp (23.5 mg, 0.0550 mmol, 1.1 eq.) and $CuBr_2$ (11.2 mg, 0.0500 mmol, 1 eq.) were diluted in MeCN (1 mL) and the complex was precipitated by addition of Et_2O (15 mL). The supernatant solution was decanted and after that the complex was again diluted in MeCN (1 mL). By slow diffusion of Et_2O (10 mL) crystals suitable for X-ray diffraction were obtained. **Yield:** 13.0 mg (0.0200 mmol, 37%), **IR** (Diamond-ATR, neat) $\tilde{\nu}_{max}$: 2928 (w, $\nu(CH_{aliph.})$), 2890 (w, $\nu(CH_{aliph.})$), 2858 (w, $\nu(CH_{aliph.})$), 1616 (vs), 1570 (vs), 1528 (vs, ν(C=N)), 1478 (m), 1440 (m), 1426 (m), 1388 (vs), 1347 (m), 1332 (w), 1278 (m), 1233 (m), 1159 (w), 1147 (m), 1098 (w), 1071 (w), 1018 (vs), 994 (m), 963 (m), 925 (w), 898 (w), 834 (vs), 764 (w), 719 (w), 686 (w), 606 (w), 557 (w), 525 (w), 481 (w), 461 (m), 397 (w), 353 (w) cm^{-1}. **EA** calcd for $C_{23}H_{38}Br_2CuN_8$ [M]: C 42.5%, H 5.9%, N 17.2%; found: C 42.4%, H 5.8%, N 17.3%. **HRMS** (ESI^+, MeCN) *m*/*z*: isotopic distribution calcd for $C_{23}H_{38}BrCuN_8$ $[M - Br]^+$: 568.1700 (69) $[C_{23}H_{38}{}^{79}Br^{63}CuN_8]^+$; 596.1727 (20) $[C_{22}{}^{13}CH_{38}{}^{79}Br^{63}CuN_8]^+$, 570.1685 (100) $[C_{23}H_{38}{}^{81}Br^{63}CuN_8]^+$, 571.1710 (28) $[C_{22}{}^{13}CH_{38}{}^{81}Br^{63}CuN_8]^+$, 572.1674 (34) $[C_{23}H_{38}{}^{81}Br^{65}CuN_8]^+$, 573.1695 (9) $[C_{22}{}^{13}CH_{38}{}^{81}Br^{65}CuN_8]^+$, found: 568.1692 (74), 569.1720 (20), 570.1676 (100), 571.1701 (29), 572.1659 (33), 573.1683 (9).

Additional information on the synthesis of the target compound and original analysis data files are available *via* Chemotion Repository: **https://dx.doi.org/10.14272/reaction/SA-FUHFF-UHFFFADPSC-NWKNMQBGGX-UHFFFADPSC-NUHFF-LUHFF-NUHFF-ZZZ**.

[Cu(TMG-4NMe$_2$uns-penp)Cl]Cl (C2). TMG-4NMe$_2$uns-penp (23.5 mg, 0.0550 mmol, 1.1 eq.) and $CuCl_2$ (6.7 mg, 0.0500 mmol, 1 eq.) were diluted in MeCN (1 mL) and the complex was precipitated by addition of Et_2O (15 mL). The supernatant solution was decanted and after that the complex was again diluted in MeCN (1 mL). By slow diffusion of Et_2O (10 mL) crystals suitable for X-ray diffraction were obtained. **Yield:** 6.7 mg (0.012 mmol, 24%), **IR** (Diamond-ATR, neat) $\tilde{\nu}_{max}$: 3380 (vw), 2895 (w, $\nu(CH_{aliph.})$), 1614 (vs), 1570 (s), 1523 (vs, ν(C=N)), 1478 (m), 1441 (m), 1426 (m), 1388 (vs), 1347 (m), 1332 (w), 1305 (m), 1279 (m), 1265 (m), 1233 (m), 1158

(w), 1146 (m), 1099 (w), 1070 (w), 1020 (vs), 963 (m), 926 (w), 899 (w), 849 (m), 836 (s), 812 (w), 764 (w), 719 (vw), 686 (w), 606 (w), 556 (w), 524 (w), 481 (w), 459 (m), 403 (w), 358 (w) cm^{-1}. **EA** calcd for $C_{23}H_{42}Cl_2CuN_8O_2$ [M + $2H_2O$]: C 46.3%, H 7.1%, N 18.8%; found: C 46.2%, H 7.0%, N 18.4%. **HRMS** (ESI^+, MeCN) *m*/*z*: isotopic distribution calcd for $C_{23}H_{38}ClCuN_8$ [M − Cl]$^+$: 524.2201 (100) $[C_{23}H_{38}{}^{35}Cl^{63}CuN_8]^+$; 525.2229 (29) $[C_{22}{}^{13}CH_{38}{}^{35}Cl^{63}CuN_8]^+$, 526.2187 (81) $[C_{23}H_{38}{}^{35}Cl^{65}CuN_8]^+$, 527.2212 (23) $[C_{22}{}^{13}CH_{38}{}^{35}Cl^{65}CuN_8]^+$, 528.2173 (18) $[C_{23}H_{38}{}^{37}Cl^{65}CuN_8]^+$, 529.2185 (4) $[C_{22}{}^{13}CH_{38}{}^{37}Cl^{65}CuN_8]^+$, 530.2208 (1) $[C_{21}{}^{13}C_2H_{38}{}^{37}Cl^{65}CuN_8]^+$, found: 524.2188 (100), 525.2209 (34), 526.2168 (78), 527.2185 (26), 528.2152 (17), 529.2154 (8), 530.2171 (2).

Additional information on the synthesis of the target compound and original analysis data files are available *via* Chemotion Repository: **https://dx.doi.org/10.14272/reaction/SA-FUHFF-UHFFFADPSC-RUGUWNHIXP-UHFFFADPSC-NUHFF-LUHFF-NUHFF-ZZZ.**

[Cu(TMG-uns-penp)Br]Br (C3). TMG-uns-penp (18.7 mg, 0.0550 mmol, 1.1 eq.) and $CuBr_2$ (11.2 mg, 0.0500 mmol, 1 eq.) were diluted in MeCN (1 mL) and the complex was precipitated by addition of Et_2O (15 mL). The supernatant solution was decanted and after that the complex was again diluted in MeCN (1 mL). By slow diffusion of Et_2O (15 mL), crystals suitable for X-ray diffraction were obtained. **Yield**: 10.2 mg (0.0181 mmol, 36%), **IR** (Diamond-ATR, neat) $\tilde{\nu}_{max}$: 3410 (vw), 2930 (vw, $\nu(CH_{aliph.})$), 2911 (vw, $\nu(CH_{aliph.})$), 2863 (vw, $\nu(CH_{aliph.})$), 1600 (w), 1558 (m, $\nu(C{=}N)$), 1476 (w), 1448 (m), 1423 (w), 1394 (m), 1343 (w), 1300 (m), 1288 (m), 1231 (vs), 1184 (m), 1152 (s), 1100 (s), 1077 (m), 1032 (w), 983 (m), 951 (w), 920 (vw), 895 (w), 857 (vw), 842 (w), 824 (w), 806 (w), 771 (m), 741 (m), 723 (w), 648 (m), 635 (m), 588 (w), 555 (m), 516 (m), 479 (m), 467 (w), 420 (m), 403 (m), 385 (w), 354 (m), 291 (m) cm^{-1}. **HRMS** (ESI^+, MeCN) *m*/*z*: isotopic distribution calcd for $C_{19}H_{28}BrCuN_6$ [M − Br]$^+$: 482.0859 (69) $[C_{19}H_{28}{}^{79}Br^{63}CuN_6]^+$; 483.0883 (16) $[C_{18}{}^{13}CH_{28}{}^{79}Br^{63}CuN_6]^+$, 484.0838 (100) $[C_{19}H_{28}{}^{81}Br^{63}CuN_6]^+$, 485.0862 (23) $[C_{18}{}^{13}CH_{28}{}^{81}Br^{63}CuN_6]^+$, 486.0821 (33) $[C_{19}H_{28}{}^{81}Br^{65}CuN_6]^+$, 487.0842 (7) $[C_{18}{}^{13}CH_{28}{}^{81}Br^{65}CuN_6]^+$, found: 482.0848 (70), 483.0876 (17), 484.0829 (100), 485.0857 (24), 486.0814 (32), 487.0832 (8).

Additional information on the synthesis of the target compound and original analysis data files are available *via* Chemotion Repository: **https://dx.doi.org/10.14272/reaction/SA-FUHFF-UHFFFADPSC-XVFHQFWAYX-UHFFFADPSC-NUHFF-LUHFF-NUHFF-ZZZ.**

[Cu(TMG$_3$tren)Br]Br (C4). TMG$_3$tren (24.2 mg, 0.0550 mmol, 1.1 eq.) and $CuBr_2$ (11.2 mg, 0.0500 mmol, 1 eq.) were diluted in MeCN (1 mL) and the complex was precipitated by addition of Et_2O (15 mL). The supernatant solution was decanted and after that the complex was again diluted in MeCN (1 mL). By slow diffusion of Et_2O (10 mL), crystals suitable for X-ray diffraction were obtained. **Yield**: 10.2 mg (0.0154 mmol, 30%), **IR** (Diamond-ATR, neat) $\tilde{\nu}_{max}$: 2959 (w, $\nu(CH_{aliph.})$), 2884 (w, $\nu(CH_{aliph.})$), 2842 (w, $\nu(CH_{aliph.})$), 1574 (m), 1550 (vs, $\nu(C{=}N)$), 1529 (s), 1483 (m), 1460 (m), 1441 (m), 1424 (m), 1392 (vs), 1344 (m), 1329 (m), 1246 (m), 1234 (w), 1213 (w), 1163 (m), 1150 (m), 1130 (w), 1079 (m), 1068 (m), 1040 (m), 1011 (m), 944 (w), 910 (m), 901 (m), 762 (m), 745 (w), 724 (w), 595 (w), 561 (w), 541 (w), 423 (m), 398 (w), 355 (m), 339 (m), 278 (m) cm^{-1}. **EA** calcd for $C_{21}H_{48}Br_2CuN_{10}$ [M]: C 38.0%, H 7.3%, N 21.1%; found: C 37.7%, H 7.0%, N 21.1%. **HRMS** (ESI^+, MeCN) *m*/*z*: isotopic distribution calcd for $C_{21}H_{48}BrCuN_{10}$ [M − Br]$^+$: 582.2546 (68) $[C_{21}H_{48}{}^{79}Br^{63}CuN_{10}]^+$; 583.2568 (19) $[C_{20}{}^{13}CH_{48}{}^{79}Br^{63}CuN_{10}]^+$, 584.2525 (100) $[C_{21}H_{48}{}^{81}Br^{63}CuN_{10}]^+$, 585.2546 (27) $[C_{20}{}^{13}CH_{48}{}^{81}Br^{63}CuN_{10}]^+$, 586.2509 (33) $[C_{21}H_{48}{}^{81}Br^{65}CuN_{10}]^+$, 587.2527 (8) $[C_{20}{}^{13}CH_{48}{}^{81}Br^{65}CuN_{10}]^+$, found: 582.2537 (64), 583.2564 (14), 584.2517 (100), 585.2544 (23), 586.2504 (27), 587.2526 (6).

Additional information on the synthesis of the target compound and original analysis data files are available *via* Chemotion Repository: **https://dx.doi.org/10.14272/reaction/SA-FUHFF-UHFFFADPSC-PIQUIJJCAD-UHFFFADPSC-NUHFF-LUHFF-NUHFF-ZZZ.**

[Cu(TMG$_3$tren)]Br (C5). TMG$_3$tren (24.2 mg, 0.0550 mmol, 1.1 eq.) and CuBr (7.2 mg, 0.050 mmol, 1 eq.) were diluted in toluene (1 mL). The solution was layered with THF (1 mL). By diffusion with THF, crystals suitable for X-ray diffraction were obtained. **Yield**: 15.4 mg (0.0264 mmol, 52%), **IR** (Diamond-ATR, neat) $\tilde{\nu}_{max}$: 2979 (w, $\nu(CH_{aliph.})$), 2961 (w, $\nu(CH_{aliph.})$), 2921 (w, $\nu(CH_{aliph.})$), 2881 (m, $\nu(CH_{aliph.})$), 2840 (m, $\nu(CH_{aliph.})$), 2801 (w), 1564 (vs, $\nu(C{=}N)$), 1511 (s), 1486 (m), 1460 (m), 1426 (s), 1407 (m), 1383 (vs), 1349 (m), 1342 (m), 1324 (w), 1279 (w), 1246 (m), 1229 (m), 1155 (m), 1140 (m), 1117 (w), 1071 (m), 1044 (m), 1031 (w), 1017 (m), 997 (m), 938 (w), 900 (m), 879 (m), 780 (vw), 758 (m), 719 (w), 589 (w), 556 (vw), 504 (w), 403 (w), 350 (m), 266 (m) cm^{-1}. **HRMS** (ESI^+, MeCN) *m*/*z*: isotopic distribution calcd for $C_{21}H_{48}CuN_{10}$ [M − Br]$^+$: 503.3362 (100) $[C_{21}H_{48}{}^{63}CuN_{10}]^+$; 504.3380 (27) $[C_{20}{}^{13}CH_{48}{}^{63}CuN_{10}]^+$, 584.2525 (100) $[C_{21}H_{48}{}^{81}Br^{63}CuN_{10}]^+$, 505.3350 (48) $[C_{21}H_{48}{}^{65}CuN_{10}]^+$, 506.3364 (12) $[C_{20}{}^{13}CH_{48}{}^{65}CuN_{10}]^+$, 507.3393 (2) $[C_{19}{}^{13}C_2H_{48}{}^{65}CuN_{10}]^+$, found: 503.3114 (100), 504.3139 (28), 505.3096 (50), 506.3120 (12), 507.3147 (1). The bulk material was analysed with powder X-ray diffraction and was confirmed to be the desired compound (Fig. S14†).

Additional information on the synthesis of the target compound and original analysis data files are available *via* Chemotion Repository: **https://dx.doi.org/10.14272/reaction/SA-FUHFF-UHFFFADPSC-RVTCRHJVTG-UHFFFADPSC-NUHFF-MUHFF-NUHFF-ZZZ.**

Polymerisation studies

Ethyl α-bromoisobutyrate (EBiB, abcr, 98%), styrene (Acros Organics, 99% stab.) and benzonitrile (Fluka Analytical, 98%) have been purified by distillation over CaH_2. AIBN (Sigma Aldrich, 98%) as well as $CuBr_2$ (Grüssing, 98%) were used without further purification and all polymerisations were conducted with *in situ* generated catalysts.

For standard ATRP experiments, first CuBr (0.19 mmol, 1 eq.), then ligand (0.19 mmol, 1 eq.) were directly weighed into the polymerisation vessel under a nitrogen atmosphere inside a glovebox. Outside the glovebox, first styrene (19 mmol, 100

eq.), then benzonitrile (1 mL), and finally EBiB (0.19 mmol, 1 eq.) were added with gastight glass syringes using Schlenk techniques. After the addition of the initiator, the reaction was started by heating to 110 °C under vigorous stirring.

For ICAR ATRP experiments, first $CuBr_2$ (0.019 mmol, 0.1 eq.), then ligand (0.019 mmol, 0.1 eq.) were directly weighed into the polymerisation vessel under a nitrogen atmosphere inside a glovebox. Outside the glovebox, styrene (19 mmol, 100 eq.), benzonitrile (1 mL), EBiB (0.19 mmol, 1 eq.) and finally AIBN (0.29 mmol, 1.5 eq.) were added with gastight glass syringes using Schlenk techniques. After three cycles of freeze–pump–thaw, the reaction was started by heating to 60 °C under vigorous stirring.

For standard ATRP and ICAR ATRP experiments, the first aliquot was taken with a glass pipette under inert conditions after 2.5 min. At this point, the polymerisation mixture reached its desired temperature and thus was chosen as the starting point of the polymerisation. Further samples were taken at certain time intervals. The samples were diluted in $CDCl_3$, and the conversion was measured *via* ^{1}H NMR spectroscopy. Afterwards, for the ICAR ATRP experiments, the polymer was precipitated in ethanol to remove the copper complex and residual monomer. The solid, colourless polystyrene was dried overnight at 50 °C, and the molecular mass and dispersity were measured by SEC.

Physical methods

X-ray diffraction analysis. The single crystal diffraction data are presented in Tables S1 and S2.† The data for **L1** were collected with a Bruker D8 goniometer with APEX CCD detector using an Incoatec microsource with Mo-K_α radiation (λ = 0.71073 Å) at 100 K in ω-scan mode. Temperature control was achieved with an Oxford Cryostream 700. Data were collected with SMART, integrated with SAINT and absorption corrected with SADABS.[104]

Data of **C1**, **C2**, **C3**, **C4** and **C5** were collected with a four-circle goniometer Stoe Stadivari equipped with a Dectris Pilatus3 R 200 K hybrid pixel detector using a GeniX 3D high flux157 Mo-K_α source (λ = 0.71073 Å) at 100 K. Temperature control was achieved with an Oxford Cryostream 800. Data were collected with X-Area Pilatus[105] and integrated with X-Area Integrate[106] and X-Area Recipe.[107] The absorption correction was performed with Stoe X-Red32, afterwards scaling of reflections with X-Area LANA was performed.[105]

The structures were solved by direct and conventional Fourier methods and all non-hydrogen atoms were refined anisotropically with full-matrix least-squares based on F^2 (XPREP,[108] SHELXS[109] and ShelXle[110]). Hydrogen atoms were derived from difference Fourier maps and placed at idealised positions, riding on their parent C atoms, with isotropic displacement parameters $U_{iso}(H) = 1.2\ U_{eq}(C)$ and $1.5\ U_{eq}(C_{methyl})$. All methyl groups were allowed to rotate but not to the tip.

In the complex **C5**, it was not possible to model the disordered solvent molecules (one molecule toluene) in an adequate manner, and the data set was treated with the SQUEEZE routine as implemented in PLATON.[111,112]

Full crystallographic data have been deposited with the Cambridge Crystallographic Data Centre as supplementary no. CCDC 2289693 for **L1**, 2289694 for **C1**, 2289695 for **C2**, 2289696for **C3**, 2289697 for **C4** and 2289698 for **C5**.†

UV/Vis spectroscopy. UV/Vis spectroscopic measurements were performed with an Agilent Technologies Cary 60 UV/Vis spectrophotometer. The measurements of the samples were performed in Hellma QS cuvettes with an optical path length of 10 mm. The titration experiments were performed in a commercial Schlenk measurement cell and the spectra were obtained with a quartz glass immersion probe (Helma, 1.00 mm, connected *via* a Cary 50 fiber optic coupler).

The titration experiment started with 5 mL of 5 mM $CuBr_2$ in MeCN. After the addition of aliquots (56 µL, 0.1 eq.) of 44 mM **L1** in MeCN, the solution was stirred for 30 s until the UV/Vis spectrum was measured.

EPR spectroscopy. The EPR spectrum was measured with a Magnetech Mini Scope MS 400. The setup included the Resonator Rectangular TE102 and a microwave frequency counter Magnetech FC. The measurement was performed in an EPR tube, closed with Critoseal® wax. The 5 mM complex solutions were prepared *in situ* by dissolution of the ligand and $CuBr_2$ in the solvent and cooled to 77 K. The following experimental parameters were chosen: microwave frequency of 9.4 ± 0.1 GHz, B_0 field 335 mT, B_0 sweep 100.1898 mT, and modulation amplitude 0.45 mT. The spectrum was simulated with the Matlab tool EasySpin[83] to obtain further information about the spin system. The applied simulation function was "pepper" which is a function for solid state continuous wave EPR with arbitrary number of spins. The spin was simulated with isotropic *g*-tensors.

Cyclic voltammetry (CV) measurements. The CV measurements were conducted at room temperature under a nitrogen atmosphere in a glovebox with a Metrohm Autolab Potentiostat PGSTAT 101 using a three electrode arrangement with a glassy carbon counter electrode, a Pt disc working electrode (1 mm diameter) and a Ag wire as the reference electrode (pseudo reference). The measurements were performed in MeCN containing 0.1 mol L^{-1} NBu_4PF_6 with a sample concentration of 1 mM. Ferrocene was added afterwards as an internal standard of the sample and all redox potentials are referenced relative to the Fc/Fc^+ couple. Cyclic voltammograms were measured with 200 mV s^{-1}, 100 mV s^{-1}, 50 mV s^{-1} and 20 mV s^{-1}. For data acquisition and analysis, the NOVA 2.1 (Build 5763) software was used.

NMR spectroscopy. ^{1}H NMR and ^{13}C NMR spectra were measured on a Bruker Avance III HD 400 or a Bruker Avance II 400 nuclear resonance spectrometer. Measurements were conducted in deuterated solvents at 25 °C. Resonances were referenced to the residual solvent resonances, relative to TMS. Chemical shifts were assigned with the use of two-dimensional NMR experiments (COSY, HSQC, HMBC). For the Bruker Avance III HD 400, the software Topspin (Version 3.5 pl 7) from Bruker and for the Bruker Avance II 400 the software TopSpin (Version 2.1) from Bruker were used for data acquisition. For visualization and examination of the NMR spectra,

the software MestReNova (Version 12.0.1-20560) from Mestrelab Research was used. All NMR spectroscopic data were deposited as original data in the Chemotion Repository and are published under an Open Access model.[113] The link to the original data is given in the analytical description. NMR spectra of the compounds are also shown (see Fig. S10–S12†).

Gel permeation chromatography (GPC). The average molecular masses and the dispersities of the obtained polystyrene samples were measured by SEC in THF as the mobile phase at a flow rate of 1 mL min^{-1}. The utilised GPCmax VE-2001 from Viscotek is a combination of two Malvern Viscotek T columns (porous styrene divinylbenzene copolymer) with a maximum pore size of 500 and 5000 Å, an HPLC pump and a refractive index detector (VE-3580) and a viscometer (Viscotek 270 Dual Detector). Universal calibration was applied to evaluate the chromatographic results. The program OmniSEC 5.12 was used for integration and data analysis.

Elemental analysis (EA). Elemental analysis was conducted with an elementar vario EL and an elementar vario EL cube or was conducted with a Unicube from Elementar.

PXRD. PXRD experiments were performed under ambient conditions on flat samples using a STOE STADI P diffractometer with the Debye–Scherrer geometry (Cu-$K_{\alpha1}$ radiation λ = 1.540598 Å, STOE image plate detector IP-PSD).

IR spectroscopy. ATR FT IR spectra were measured with a Shimadzu IRTracer 100 with CsI beam splitter in combination with a Specac Quest ATR unit utilising a robust monolithic crystalline diamond (resolution: 2 cm^{-1}). The program LabSolution IR (Version 2.15) from SHIMADZU was used. All IR spectroscopic data were deposited as original data in the Chemotion Repository and are published under an Open Access model.[113]

Mass spectrometry (MS). Electron spray ionization mass spectrometry (ESI-MS) measurements were performed on an UHR-TOF Bruker Daltonik maXis II, an ESI-quadrupole time-of-flight (qToF) mass spectrometer capable of a resolution of at least 80.000 FWHM. Detection was in either the positive or negative ion mode. The mass spectrometer was calibrated subsequently to every experiment *via* direct infusion of a L proline sodium salt solution, which provided a *m*/*z* range of singly charged peaks up to 3000 Da in both ion modes. The data were collected with the program otofControl and processed in Compass DataAnalysis. All MS spectrometric data were deposited as original data in the Chemotion Repository and are published under an Open Access model.[113]

DFT calculation. Density functional theory (DFT) calculations were performed with Gaussian 16, Revision B.01, using the default UltraFine grid (a 99 590 grid).[114] The geometry optimisations were started from the geometry of the solid state structures of the cationic units if available using the TPSSh functional[90,91] and with the Ahlrichs type basis set def2-TZVP[92–95] as implemented in Gaussian 16, Revision B.01.[114] As solvent model, the Polarizable Continuum Model (PCM) was used as implemented in Gaussian 16. As empirical dispersion correction, the D3 version of Grimme's dispersion with Becke–Johnson damping (GD3BJ) was used as implemented in Gaussian16, Revision B.01.[96–98] Frequency calculations did not show imaginary values. Additionally a Conformer-Rotamer Ensemble Sampling Tool (CREST) calculation of the complex cation of **C1** was performed to verify the minimum found in the DFT optimization (Version 2.12).[115,116] NBO calculations were accomplished using the program suite NBO 7.0 delivering the NBO charges and the charge-transfer energies by second-order perturbation theory.[117–119] For visualization and extraction of the calculated structural information, GaussView (Version 6.0.16) was used. The calculated energy values and NBO results were extracted directly from the output files using notepad++ (Version 7.8.1).

Conflicts of interest

There are no conflicts to declare.

Acknowledgements

S. H–P. is thankful for the generous funding by the Deutsche Forschungsgemeinschaft within the collaborative research centre CRC985 (project INF). We thank NFDI4Chem for support and funding of the repository. Moreover, we thank Prof. Dr Schindler's working group (Justus Liebig University Gießen) for providing the amine precursor for the subsequent guanidine synthesis of TMG-uns-penp (**L2**). The authors would also like to thank Patrick Schumann for his support as a research assistant. We furthermore thank the Regional Computing Center of the University of Cologne (RRZK) for providing the computing time on the DFG-funded High Performance Computing (HPC) system CHEOPS as well as support.

References

1 J. S. Wang and K. Matyjaszewski, *J. Am. Chem. Soc.*, 1995, **117**, 5614–5615.
2 J.-S. Wang and K. Matyjaszewski, *Macromolecules*, 1995, **28**, 7901–7910.
3 M. Kato, M. Kamigaito, M. Sawamoto and T. Higashimura, *Macromolecules*, 1995, **28**, 1721–1723.
4 V. Percec and B. Barboiu, *Macromolecules*, 1995, **28**, 7970–7972.
5 K. Matyjaszewski, *Adv. Mater.*, 2018, **30**, 1706441.
6 M. Kamigaito, T. Ando and M. Sawamoto, *Chem. Rev.*, 2001, **101**, 3689–3746.
7 K. Matyjaszewski and J. Xia, *Chem. Rev.*, 2001, **101**, 2921–2990.
8 J. Xia, S. G. Gaynor and K. Matyjaszewski, *Macromolecules*, 1998, **31**, 5958–5959.
9 J. Xia and K. Matyjaszewski, *Macromolecules*, 1999, **32**, 2434–2437.
10 T. Pintauer and K. Matyjaszewski, *Chem. Soc. Rev.*, 2008, **37**, 1087–1097.

11 T. G. Ribelli, F. Lorandi, M. Fantin and K. Matyjaszewski, *Macromol. Rapid Commun.*, 2019, **40**, 1800616.
12 K. Matyjaszewski and A. H. E. Müller, *Controlled and Living Polymerizations: From Mechanisms to Applications*, Wiley-VCH, Weinheim, 2009.
13 C. Y. Lin, M. L. Coote, A. Gennaro and K. Matyjaszewski, *J. Am. Chem. Soc.*, 2008, **130**, 12762–12774.
14 K. Matyjaszewski, *Macromolecules*, 2012, **45**, 4015–4039.
15 V. Coessens, T. Pintauer and K. Matyjaszewski, *Prog. Polym. Sci.*, 2001, **26**, 337–377.
16 H. Fischer, *J. Polym. Sci., Part A: Polym. Chem.*, 1999, **37**, 1885–1901.
17 H. Mohapatra, M. Kleiman and A. P. Esser-Kahn, *Nat. Chem.*, 2017, **9**, 135–139.
18 Z. Wang, X. Pan, J. Yan, S. Dadashi-Silab, G. Xie, J. Zhang, Z. Wang, H. Xia and K. Matyjaszewski, *ACS Macro Lett.*, 2017, **6**, 546–549.
19 Y. Sun, S. Lathwal, Y. Wang, L. Fu, M. Olszewski, M. Fantin, A. E. Enciso, G. Szczepaniak, S. Das and K. Matyjaszewski, *ACS Macro Lett.*, 2019, **8**, 603–609.
20 P. Chmielarz, M. Fantin, S. Park, A. A. Isse, A. Gennaro, A. J. D. Magenau, A. Sobkowiak and K. Matyjaszewski, *Prog. Polym. Sci.*, 2017, **69**, 47–78.
21 D. Konkolewicz, Y. Wang, M. Zhong, P. Krys, A. A. Isse, A. Gennaro and K. Matyjaszewski, *Macromolecules*, 2013, **46**, 8749–8772.
22 M. R. Martinez, J. Sobieski, F. Lorandi, M. Fantin, S. Dadashi-Silab, G. Xie, M. Olszewski, X. Pan, T. G. Ribelli and K. Matyjaszewski, *Macromolecules*, 2020, **53**, 59–67.
23 M. Rolland, R. Whitfield, D. Messmer, K. Parkatzidis, N. P. Truong and A. Anastasaki, *ACS Macro Lett.*, 2019, **8**, 1546–1551.
24 X. Pan, M. A. Tasdelen, J. Laun, T. Junkers, Y. Yagci and K. Matyjaszewski, *Prog. Polym. Sci.*, 2016, **62**, 73–125.
25 W. Jakubowski and K. Matyjaszewski, *Angew. Chem., Int. Ed.*, 2006, **45**, 4482–4486, (*Angew. Chem.*, 2006, **118**, 4594–4598).
26 V. A. Williams, T. G. Ribelli, P. Chmielarz, S. Park and K. Matyjaszewski, *J. Am. Chem. Soc.*, 2015, **137**, 1428–1431.
27 T. G. Ribelli, M. Fantin, J.-C. Daran, K. F. Augustine, R. Poli and K. Matyjaszewski, *J. Am. Chem. Soc.*, 2018, **140**, 1525–1534.
28 K. Matyjaszewski, W. Jakubowski, K. Min, W. Tang, J. Huang, W. A. Braunecker and N. V. Tsarevsky, *Proc. Natl. Acad. Sci. U. S. A.*, 2006, **103**, 15309–15314.
29 D. Konkolewicz, A. J. D. Magenau, S. E. Averick, A. Simakova, H. He and K. Matyjaszewski, *Macromolecules*, 2012, **45**, 4461–4468.
30 A. E. Enciso, F. Lorandi, A. Mehmood, M. Fantin, G. Szczepaniak, B. G. Janesko and K. Matyjaszewski, *Angew. Chem., Int. Ed.*, 2020, **59**, 14910–14920, (*Angew. Chem.*, 2020, **132**, 15020–15030).
31 E. Mastan and S. Zhu, *Macromolecules*, 2015, **48**, 6440–6449.
32 P. Krys and K. Matyjaszewski, *Eur. Polym. J.*, 2017, **89**, 482–523.
33 V. Doan, B. B. Noble, A. K. K. Fung and M. L. Coote, *J. Org. Chem.*, 2019, **84**, 15624–15632.
34 T. G. Ribelli, F. Lorandi, M. Fantin and K. Matyjaszewski, *Macromol. Rapid Commun.*, 2019, **40**, 1800616.
35 M. Fantin, F. Lorandi, T. G. Ribelli, G. Szczepaniak, A. E. Enciso, C. Fliedel, L. Thevenin, A. A. Isse, R. Poli and K. Matyjaszewski, *Macromolecules*, 2019, **52**, 4079–4090.
36 L. Thevenin, C. Fliedel, K. Matyjaszewski and R. Poli, *Eur. J. Inorg. Chem.*, 2019, **2019**, 4489–4499.
37 N. V. Tsarevsky, W. A. Braunecker, A. Vacca, P. Gans and K. Matyjaszewski, *Macromol. Symp.*, 2007, **248**, 60–70.
38 W. Tang, Y. Kwak, W. Braunecker, N. V. Tsarevsky, M. L. Coote and K. Matyjaszewski, *J. Am. Chem. Soc.*, 2008, **130**, 10702–10713.
39 N. V. Tsarevsky, W. A. Braunecker and K. Matyjaszewski, *J. Organomet. Chem.*, 2007, **692**, 3212–3222.
40 N. V. Tsarevsky and K. Matyjaszewski, *Chem. Rev.*, 2007, **107**, 2270–2299.
41 P. Paoli, A. Isse, N. Bortolamei and A. Gennaro, *Chem. Commun.*, 2011, **47**, 3580–3582.
42 N. Bortolamei, A. A. Isse, V. B. Di Marco, A. Gennaro and K. Matyjaszewski, *Macromolecules*, 2010, **43**, 9257–9267.
43 N. V. Tsarevsky, T. Pintauer and K. Matyjaszewski, *Macromolecules*, 2004, **37**, 9768–9778.
44 F. di Lena and K. Matyjaszewski, *Prog. Polym. Sci.*, 2010, **35**, 959–1021.
45 W. Tang and K. Matyjaszewski, *Macromolecules*, 2006, **39**, 4953–4959.
46 K. Matyjaszewski, B. Göbelt, H.-J. Paik and C. P. Horwitz, *Macromolecules*, 2001, **34**, 430–440.
47 F. Lorandi and K. Matyjaszewski, *Isr. J. Chem.*, 2020, **60**, 108–123.
48 J. Stanek, T. Rösener, A. Metz, J. Mannsperger, A. Hoffmann and S. Herres-Pawlis, in *Guanidines as Reagents and Catalysts II*, ed. P. Selig, Springer International Publishing, Cham, 2017, pp. 95–164.
49 T. Rösener, O. Bienemann, K. Sigl, N. Schopp, F. Schnitter, U. Flörke, A. Hoffmann, A. Döring, D. Kuckling and S. Herres-Pawlis, *Chem. – Eur. J.*, 2016, **22**, 13550–13562.
50 K. W. Kröckert, J. S. Mannsperger, T. Rösener, A. Hoffmann and S. Herres-Pawlis, *Z. Anorg. Allg. Chem.*, 2021, **647**, 832–842.
51 T. Rösener, A. Hoffmann and S. Herres-Pawlis, *Eur. J. Inorg. Chem.*, 2018, **2018**, 3164–3175.
52 T. Rösener, K. Kröckert, A. Hoffmann and S. Herres-Pawlis, *Z. Anorg. Allg. Chem.*, 2018, **644**, 1317–1328.
53 R. D. Rittinghaus, A. Karabulut, A. Hoffmann and S. Herres-Pawlis, *Angew. Chem., Int. Ed.*, 2021, **60**, 21795–21800, (*Angew. Chem.*, 2021, **133**, 21965–21971).
54 A. Hermann, S. Hill, A. Metz, J. Heck, A. Hoffmann, L. Hartmann and S. Herres-Pawlis, *Angew. Chem., Int. Ed.*, 2020, **59**, 21778–21784.
55 R. D. Rittinghaus, J. Zenner, A. Pich, M. Kol and S. Herres-Pawlis, *Angew. Chem., Int. Ed.*, 2022, **61**, e202112853, (*Angew. Chem.*, 2022, **134**, e202112853).

56 M. Paul, A. Hoffmann and S. Herres-Pawlis, *J. Biol. Inorg. Chem.*, 2021, **26**, 249–263.
57 M. Paul, M. Teubner, B. Grimm-Lebsanft, S. Buchenau, A. Hoffmann, M. Rübhausen and S. Herres-Pawlis, *J. Inorg. Biochem.*, 2021, **224**, 111541.
58 M. Paul, M. Teubner, B. Grimm-Lebsanft, C. Golchert, Y. Meiners, L. Senft, K. Keisers, P. Liebhäuser, T. Rösener, F. Biebl, S. Buchenau, M. Naumova, V. Murzin, R. Krug, A. Hoffmann, J. Pietruszka, I. Ivanović-Burmazović, M. Rübhausen and S. Herres-Pawlis, *Chem. – Eur. J.*, 2020, **26**, 7556–7562.
59 J. Heck, F. Metz, S. Buchenau, M. Teubner, B. Grimm-Lebsanft, T. P. Spaniol, A. Hoffmann, M. A. Rübhausen and S. Herres-Pawlis, *Chem. Sci.*, 2022, **13**, 8274–8288.
60 B. Dicke, A. Hoffmann, J. Stanek, M. S. Rampp, B. Grimm-Lebsanft, F. Biebl, D. Rukser, B. Maerz, D. Göries, M. Naumova, M. Biednov, G. Neuber, A. Wetzel, S. M. Hofmann, P. Roedig, A. Meents, J. Bielecki, J. Andreasson, K. R. Beyerlein, H. N. Chapman, C. Bressler, W. Zinth, M. Rübhausen and S. Herres-Pawlis, *Nat. Chem.*, 2018, **10**, 355–362.
61 K. W. Kröckert, F. Garg, M. V. Heinz, J. Lange, P. P. Simões, R. Schmidt, O. Bienemann, A. Hoffmann and S. Herres-Pawlis, *Dalton Trans.*, 2022, **51**, 13272–13287.
62 L. I. Manasieva, B. U. Maria, A. Prandi, L. Brasili and S. Franchini, *Synthesis*, 2015, **47**, 3767–3775.
63 R. L. Lucas, M. K. Zart, J. Murkerjee, T. N. Sorrell, D. R. Powell and A. S. Borovik, *J. Am. Chem. Soc.*, 2006, **128**, 15476–15489.
64 M. Mori, M. C. Dasso Lang, F. Saladini, N. Palombi, L. Kovalenko, D. De Forni, B. Poddesu, L. Friggeri, A. Giannini, S. Malancona, V. Summa, M. Zazzi, Y. Mely and M. Botta, *ACS Med. Chem. Lett.*, 2019, **10**, 463–468.
65 J. England, R. Gondhia, L. Bigorra-Lopez, A. R. Petersen, A. J. P. White and G. J. P. Britovsek, *Dalton Trans.*, 2009, 5319–5334.
66 S. Herres-Pawlis, U. Flörke and G. Henkel, *Eur. J. Inorg. Chem.*, 2005, **2005**, 3815–3824.
67 W. Kantlehner, E. Haug, W. W. Mergen, P. Speh, T. Maier, J. J. Kapassakalidis, H.-J. Bräuner and H. Hagen, *Liebigs Ann. Chem.*, 1984, **1984**, 108–126.
68 J. B. Mandel, C. Maricondi and B. E. Douglas, *Inorg. Chem.*, 1998, **27**, 2990–2996.
69 R. Wortmann, Dissertation, Universität Paderborn, 2011.
70 H. Wittmann, V. Raab, A. Schorm, J. Plackmeyer and J. Sundermeyer, *Eur. J. Inorg. Chem.*, 2001, **2001**, 1937–1948.
71 A. W. Addison, T. N. Rao, J. Reedijk, J. van Rijn and G. C. Verschoor, *J. Chem. Soc., Dalton Trans.*, 1984, 1349–1356.
72 L. Yang, D. R. Powell and R. P. Houser, *Dalton Trans.*, 2007, 955–964.
73 A. J. D. Magenau, Y. Kwak, K. Schröder and K. Matyjaszewski, *ACS Macro Lett.*, 2012, **1**, 508–512.
74 L. A. van de Kuil, H. Luitjes, D. M. Grove, J. W. Zwikker, J. G. M. van der Linden, A. M. Roelofsen, L. W. Jenneskens, W. Drenth and G. van Koten, *Organometallics*, 1994, **13**, 468–477.
75 H. Nitadori, T. Takahashi, A. Inagaki and M. Akita, *Inorg. Chem.*, 2012, **51**, 51–62.
76 V. Raab, K. Harms, J. Sundermeyer, B. Kovačević and Z. B. Maksić, *J. Org. Chem.*, 2003, **68**, 8790–8797.
77 W. T. Eckenhoff and T. Pintauer, *Dalton Trans.*, 2011, **40**, 4909–4917.
78 W. T. Eckenhoff, S. T. Garrity and T. Pintauer, *Eur. J. Inorg. Chem.*, 2008, **2008**, 563–571.
79 W. T. Eckenhoff and T. Pintauer, *Inorg. Chem.*, 2010, **49**, 10617–10626.
80 O. Bienemann, A. Hoffmann and S. Herres-Pawlis, *Rev. Inorg. Chem.*, 2011, **31**, 83–108.
81 M. A. Hiskey and R. R. Ruminski, *Inorg. Chim. Acta*, 1986, **112**, 189–195.
82 G. A. McLachlan, G. D. Fallon, R. L. Martin and L. Spiccia, *Inorg. Chem.*, 1995, **34**, 254–261.
83 S. Stoll and A. Schweiger, *J. Magn. Reson.*, 2006, **178**, 42–55.
84 J. Peisach and W. E. Blumberg, *Arch. Biochem. Biophys.*, 1974, **165**, 691–708.
85 A. Kaur, T. G. Ribelli, K. Schröder, K. Matyjaszewski and T. Pintauer, *Inorg. Chem.*, 2015, **54**, 1474–1486.
86 N. G. Connelly and W. E. Geiger, *Chem. Rev.*, 1996, **96**, 877–910.
87 V. Balland, C. Hureau and J.-M. Savéant, *Proc. Natl. Acad. Sci. U. S. A.*, 2010, **107**, 17113–17118.
88 J. Qiu, K. Matyjaszewski, L. Thouin and C. Amatore, *Macromol. Chem. Phys.*, 2000, **201**, 1625–1631.
89 W. A. Braunecker, N. V. Tsarevsky, A. Gennaro and K. Matyjaszewski, *Macromolecules*, 2009, **42**, 6348–6360.
90 J. Tao, J. P. Perdew, V. N. Staroverov and G. E. Scuseria, *Phys. Rev. Lett.*, 2003, **91**, 146401.
91 V. N. Staroverov, G. E. Scuseria, J. Tao and J. P. Perdew, *J. Chem. Phys.*, 2003, **119**, 12129–12137.
92 F. Weigend and R. Ahlrichs, *Phys. Chem. Chem. Phys.*, 2005, **7**, 3297–3305.
93 A. Schäfer, C. Huber and R. Ahlrichs, *J. Chem. Phys.*, 1994, **100**, 5829–5835.
94 K. Eichkorn, F. Weigend, O. Treutler and R. Ahlrichs, *Theor. Chem. Acc.*, 1997, **97**, 119–124.
95 F. Weigend, M. Häser, H. Patzelt and R. Ahlrichs, *Chem. Phys. Lett.*, 1998, **294**, 143–152.
96 A. Hoffmann, R. Grunzke and S. Herres-Pawlis, *J. Comput. Chem.*, 2014, **35**, 1943–1950.
97 S. Grimme, S. Ehrlich and L. Goerigk, *J. Comput. Chem.*, 2011, **32**, 1456–1465.
98 L. Goerigk and S. Grimme, *Phys. Chem. Chem. Phys.*, 2011, **13**, 6670–6688.
99 P. Krys, H. Schroeder, J. Buback, M. Buback and K. Matyjaszewski, *Macromolecules*, 2016, **49**, 7793–7803.
100 F. Lorandi, M. Fantin and K. Matyjaszewski, *J. Am. Chem. Soc.*, 2022, **144**, 15413–15430.

101 N. Andre and J. M. E. Maier, *Praxis in der Organischen Chemie*, VCH, Weinheim, 1997.
102 H. Fuchida, S. Tabata, N. Shindo, I. Takashima, Q. Leng, Y. Hatsuyama, I. Hamachi and A. Ojida, *Bull. Chem. Soc. Jpn.*, 2015, **88**, 784–791.
103 H.-D. Hardt, *Z. Anorg. Allg. Chem.*, 1959, **301**, 87–96.
104 *SMART (Version 5.631), SAINT (Version 8.37A) and SADABS (Version 2008/1)*, Bruker AXS Inc., Madison, Wisconsin, USA, 2008.
105 *X-Area Pilatus3_SV 1.21.131.0*, STOE, 2017.
106 *X-Area Integrate 1.71.0.0*, STOE, 2016.
107 *X-Area Pecipe 1.33.0.0*, STOE, 2015.
108 Bruker, in *XPREP*, Bruker AXS Inc., Madison, Wisconsin, USA, 2007.
109 G. Sheldrick, *Acta Crystallogr., Sect. A: Found. Crystallogr.*, 1990, **46**, 467–473.
110 C. B. Hübschle, G. M. Sheldrick and B. Dittrich, *J. Appl. Crystallogr.*, 2011, **44**, 1281–1284.
111 A. L. Spek, *PLATON, A Multipurpose Crystallographic Tool*, Utrecht University, Utrecht (The Netherlands), 2008.
112 A. Spek, *Acta Crystallogr., Sect. D: Biol. Crystallogr.*, 2009, **65**, 148–155.
113 P. Tremouilhac, C.-L. Lin, P.-C. Huang, Y.-C. Huang, A. Nguyen, N. Jung, F. Bach, R. Ulrich, B. Neumair, A. Streit and S. Bräse, *Angew. Chem., Int. Ed.*, 2020, **59**, 22771–22778, (*Angew. Chem.*, 2006, **118**, 4594–4598).
114 M. J. Frisch, G. W. Trucks, H. B. Schlegel, G. E. Scuseria, M. A. Robb, J. R. Cheeseman, G. Scalmani, V. Barone, G. A. Petersson, H. Nakatsuji, X. Li, M. Caricato, A. V. Marenich, J. Bloino, B. G. Janesko, R. Gomperts, B. Mennucci, H. P. Hratchian, J. V. Ortiz, A. F. Izmaylov, J. L. Sonnenberg, D. Williams-Young, F. Ding, F. Lipparini, F. Egidi, J. Goings, B. Peng, A. Petrone, T. Henderson, D. Ranasinghe, V. G. Zakrzewski, J. Gao, N. Rega, G. Zheng, W. Liang, M. Hada, M. Ehara, K. Toyota, R. Fukuda, J. Hasegawa, M. Ishida, T. Nakajima, Y. Honda, O. Kitao, H. Nakai, T. Vreven, K. Throssell, J. A. Montgomery Jr., J. E. Peralta, F. Ogliaro, M. J. Bearpark, J. J. Heyd, E. N. Brothers, K. N. Kudin, V. N. Staroverov, T. A. Keith, R. Kobayashi, J. Normand, K. Raghavachari, A. P. Rendell, J. C. Burant, S. S. Iyengar, J. Tomasi, M. Cossi, J. M. Millam, M. Klene, C. Adamo, R. Cammi, J. W. Ochterski, R. L. Martin, K. Morokuma, O. Farkas, J. B. Foresman and D. J. Fox, *Gaussian 16, Revison B.01*, Gaussian, Inc., Wallingford CT, 2016.
115 P. Pracht, F. Bohle and S. Grimme, *Phys. Chem. Chem. Phys.*, 2020, **22**, 7169–7192.
116 C. Plett and S. Grimme, *Angew. Chem., Int. Ed.*, 2023, **62**, e202214477, (*Angew. Chem.*, 2023, **135**, e202214477).
117 F. Weinhold and C. R. Landis, *Valency and bonding: a natural bond orbital donor-acceptor perspective*, Cambridge University Press, 2005.
118 E. D. Glendening, J. K. Badenhoop, A. E. Reed, J. E. Carpenter, J. A. Bohmann, C. M. Morales, P. Karafiloglou, C. R. Landis and F. Weinhold, *NBO 7.0*, Theoretical Chemistry Institute, University of Wisconsin, Madison, 2018.
119 E. D. Glendening, C. R. Landis and F. Weinhold, *J. Comput. Chem.*, 2019, **40**, 2234–2241.